

The Role of Interfacial Morphology in Cu₂O/TiO₂ and Band Bending: Insights from Density Functional Theory

Mona Asadinamin,¹ Aleksandar Živkovic^{2,3}, Nora H. De Leeuw², and Steven P. Lewis¹

¹ Department of Physics and Astronomy, University of Georgia, Athens, Georgia 30602, US

² Department of Earth Sciences, Utrecht University, Princetonlaan 8a, 3548CB Utrecht, The Netherlands

³ Institut für Theoretische Physik und Astrophysik, Christian-Albrechts-Universität zu Kiel, Leibnizstraße 15, 24118 Kiel, Germany

Corresponding author: a.zivkovic@uu.nl, splewis@uga.edu

Abstract

Photocatalysis, a promising solution for environmental challenges, relies on the generation and utilization of photogenerated charge carriers within photocatalysts. However, recombination of these carriers often limits efficiency. Heterostructures, especially Cu₂O/TiO₂, have emerged as effective solutions to enhance charge separation. This study systematically explores the effect of interfacial morphologies on the band bending within Cu₂O/TiO₂ anatase heterostructures, employing density functional theory (DFT). Through this study, eight distinct interfaces are identified and analyzed, revealing a consistent staggered-type band alignment. Despite variations in band edge positions, a systematic charge transfer from Cu₂O to TiO₂ is observed across all interfaces. The proposed band bending configurations would suggest enhanced charge separation and photocatalytic activity under ultraviolet illumination due to a Z-scheme configuration. This theoretical investigation provides valuable insights into the interplay between interfacial morphology, band bending, and charge transfer, for advancing the understanding of fundamental electronic mechanisms in heterostructures.

Keywords: Heterostructures, Cu₂O/TiO₂, Anatase, Density Functional Theory, DFT, Interface, Band Bending, Z-scheme, Photocatalysis.

Introduction

Photocatalysis, a promising solution to environmental challenges like air purification and wastewater treatment, operates via the absorption of photons to create charge carriers (electron-hole pairs) within a photocatalyst. These photogenerated charge carriers are then anticipated to participate in surface redox reactions that fuel the photocatalytic process. A challenge, however, is the tendency of the photogenerated electrons and holes to recombine which deactivates the charge carriers before they can contribute to the desired photocatalytic reactions. Particularly in single photocatalysts, the lack of a suitable mechanism to efficiently separate and transport these charge carriers often leads to high recombination rates. Various strategies have been proposed to overcome these limitations, such as surface modification¹⁻³, metal or non-metal doping^{4, 5}, etc. Among these, heterostructures have emerged as effective solutions by significantly enhancing efficiency via charge separation⁶⁻⁹. Key benefits include improved separation of photogenerated charge carriers, achieved through staggered band alignments across different materials, leading to reduced recombination rates and longer charge carrier lifetimes. Furthermore, materials like TiO₂, while exhibiting excellent photocatalytic performance, suffer from a wide band gap, limiting their effectiveness under visible light. By forming heterostructures, it is possible to combine such compounds with narrow band gap materials to enhance the utilization of the visible light spectrum.

In a heterostructure, when two semiconductor materials meet at the junction, their differing energy band gaps and band edge positions cause an initial discontinuity in the fermi energy. To reach equilibrium, electrons and holes migrate in opposing directions. This charge transport gives rise to an interfacial space charge region, stemming from the electric field, which consequently results in band bending¹⁰. Depending on the relative band edges and configuration of band bending, semiconductor interfaces can be organized into four types of heterojunctions: straddling

gap (type I), staggered gap (type II), Z-scheme, or broken gap (type III)¹¹. Type II and Z-scheme interfaces can reduce electron-hole recombination and increase the migration of specific charge carriers to the semiconductor surface, enhancing photocatalytic reactions. Identifying the band bending configuration is key to predict the fundamental photocatalytic mechanisms of heterostructures.

In evaluating the band bending at interfaces, the morphology of materials can influence their interfacial band structure and band bending properties¹²⁻¹⁵. With advancements in novel growth techniques, such as molecular-beam epitaxy, epitaxial interfaces of exceptional quality can be fabricated^{16, 17}. This is achievable not just between lattice-matched semiconductors but also between materials with considerable differences in their lattice constants^{18, 19}. When these lattice mismatches are present, uniform lattice strain can accommodate them if the layers are sufficiently thin²⁰. These strains introduce alterations to electronic properties, offering enhanced versatility in designing semiconductor devices^{20, 21}. The interplay between structural and electronic properties at interfaces can be explored both experimentally and theoretically, with each technique coming with their own set of opportunities and obstacles. Density functional theory (DFT) calculations as well as experimental methods, like in situ X-ray photoelectron spectroscopy and scanning transmission electron microscopy (TEM), reveal that structural changes, including planar defects²², elastic strain²³, tensile strain²⁴, and introduction of impurities and vacancies²⁵ affect the electronic transport properties of the interface. Specifically, these changes influence band edge offsets, enabling tunable band bending properties for photocatalytic applications. However, from a computational point of view, a challenge persists in determining the precise atomic structure at interfaces given that acquiring experimental data on interfacial morphologies often proves elusive²⁶. Direct observation of interfacial atomic structures using high-resolution TEM is

challenging, primarily because of the limited reflections from lattice planes which make it difficult to ascertain actual atom positions²⁷, and high-resolution observations of these interfacial geometries remain a formidable task^{28, 29}. As a result, the detailed atomic structure and compositional data of interfaces required for precise first-principles calculations of their electronic properties is often lacking. This underscores the importance of a comprehensive theoretical investigation and systematical exploration of various interfacial morphologies, accounting for different degrees of lattice mismatch, and to analyze their impact on the electronic and band bending properties of heterostructures.

Theoretical calculations for a long time have been employed to study the electronic properties of interfaces. While earlier methods leaned on more basic techniques such as effective dipole models³⁰, tight-binding schemes³¹ or empirical rules³², in the recent few decades DFT has been utilized as an advanced computational to study band offset and interfacial dipole in heterostructures³³⁻³⁶. Despite the valuable contributions of DFT studies in this area, several limitations persist. The majority of investigations lack precise predictions due to the absence of explicit heterostructure calculations³⁷⁻⁴⁷. Additionally, many studies tend to focus on arbitrary surface orientations of the individual components rather than considering the most dominant orientations from experimental observations, and more importantly, arbitrarily chosen interfacial morphologies, which may not accurately sketch the full picture of all the possible configurations and their effect on band bending^{15, 48-53}.

In this study, two well-known photocatalysts TiO₂ and Cu₂O have been selected to study the morphological effect on their interfacial electronic properties. TiO₂ –a prominent photocatalyst due to its remarkable photocatalytic properties⁵⁴⁻⁵⁸– has been frequently paired with Cu₂O – an abundant, low-cost and well-studied effective photocatalyst⁵⁹– demonstrating enhanced charge

transfer rates and reduced electron-hole recombination^{37, 40, 54}. This heterostructure, mitigates the main drawback of TiO₂ which is its large band gap (~ 3.2 eV⁶⁰), by pairing it with Cu₂O, a lower band gap material (~ 2.2 eV⁶¹). The incorporation of Cu₂O facilitates the extension of light absorption into the visible spectrum, thereby optimizing the use of solar energy⁵⁴. Furthermore, both materials have appropriate band edges with respect to the redox potential of many pollutants^{62, 63}, facilitating the requisite redox reactions by ensuring that the photogenerated electrons in the conduction band (CB) have adequate energy for reduction reactions, while the holes in the valence band (VB) possess sufficient energy for oxidation reactions. Numerous experimental studies have been conducted to examine the interfacial band edges of Cu₂O/TiO₂. While the majority of investigations have reported a staggered (type II or Z-scheme) heterojunction featuring Cu₂O band edges situated above the TiO₂ band edges^{47, 64-80}, a limited number of studies have identified a straddling (type I) heterojunction with the VB and CB of Cu₂O positioned within the band gap of TiO₂^{54, 81}. This has led to a debate regarding the nature of the heterostructure between type II, Z-scheme, and type I configurations. Despite a great number of experimental studies, theoretical studies on Cu₂O/TiO₂ remain scarce⁸²⁻⁸⁴. Although experimental research has provided valuable insights into the interfacial properties of Cu₂O/TiO₂, a more comprehensive understanding of the electronic properties at the interface is still needed, particularly from a theoretical standpoint. In this study, we mapped all the possible interfacial morphologies of Cu₂O/TiO₂ and by assessing the chemistry of interfacial bonding, quantifying the strain magnitude, and considering the size of the system in relation to the computational feasibility, we identified eight distinct interfacial morphologies to study their band bending properties. Despite the variation in the morphology of the interfaces and the level of strain, we observed similar electronic properties and band bending behavior across all the heterostructures.

Computational Details

All calculations were carried out based on the framework of generalized Kohn-Sham scheme^{85, 86} as implemented in the Vienna ab initio simulation package (VASP)⁸⁷⁻⁸⁹, employing PBE^{90, 91} and Heyd–Scuseria–Ernzerhof (HSE06) hybrid functional⁹²⁻⁹⁴. The electron–core interactions have been described by means of the projected augmented wave (PAW) method^{89, 95}. Soft PAW potentials were used for Cu, O, and Ti atoms. The electronic wave functions were expanded in plane waves with an energy cutoff of 550 eV. The Brillouin zone was sampled using the Monkhorst–Pack special k-point mesh⁹⁶. The convergence threshold for total energy self-consistency was kept at 10^{-6} eV. The atomic coordinates and unit cell parameters have been optimized using the conjugate gradient method until the force on each atom was less than 0.01 eV \AA^{-1} . TiO₂ in its anatase phase has been used because of its superior photocatalytic activity.

The crystal configuration of Cu₂O is defined by a cubic lattice structure, characterized by Pn $\bar{3}$ m space group. Its unit cell contains four copper (Cu) and two oxygen (O) atoms. The crystal configuration of TiO₂ (titanium dioxide) in its anatase form is defined by a tetragonal lattice structure, characterized by the I41/amd space group. Its unit cell contains four titanium (Ti) and eight O atoms. The computed lattice parameters using PBE functional for Cu₂O are $a_{\text{Cu}_2\text{O}} = 4.267 \text{ \AA}$, and for TiO₂ are $a_{\text{TiO}_2} = 3.807 \text{ \AA}$, $c_{\text{TiO}_2} = 9.707 \text{ \AA}$, in good agreement with the experimental findings of $a_{\text{Cu}_2\text{O}}^{\text{exp}} \sim 4.269 \text{ \AA}$ ^{97, 98}, $a_{\text{TiO}_2}^{\text{exp}} \sim 3.78 \text{ \AA}$ ⁹⁹⁻¹⁰¹, and $c_{\text{TiO}_2}^{\text{exp}} \sim 9.50 \text{ \AA}$ ⁹⁹⁻¹⁰¹.

In order to design a realistic model system of the Cu₂O/TiO₂ heterojunction, we have considered the Cu₂O (111) and the TiO₂-anatase (101) nonpolar surfaces, being the most stable and dominant terminations across diverse morphologies and fabrication techniques^{37, 43, 54, 102-104}. The surfaces were modeled as two-dimensional periodic slabs, with a vacuum layer separating the periodic images in the z-direction. A vacuum region of at 20 \AA was tested to be sufficient to avoid

the superficial interactions between the periodic slabs. The in-plane lattice constants are fixed to the optimized bulk values and only the internal coordinates are relaxed. To characterize the surfaces, the surface energy (γ) as a measure of the thermodynamic stability has been calculated through the following expression:

$$\gamma = \frac{E(n) - nE_{\text{bulk}}}{2A}, \quad (1)$$

where $E(n)$ is the energy of the slab containing n layers, E_{bulk} the energy of the bulk, and A the area of one side of the slab.

The specific adhesive energy, a measure of the energy gained once the interface boundary between two surfaces ($s1$ and $s2$) is formed, is given by:

$$\beta_{s1/s2} = \frac{E_{s1} + E_{s2} - E_{s1/s2}}{A}, \quad (2)$$

where E_{s1} and E_{s2} are total energies of the respective slabs and $E_{s1/s2}$ is the final interface energy.

The specific interface energy, defined as the excess energy resulting from the energy balance described by the Dupré's relation¹⁰⁵, is given by:

$$\gamma_{s1/s2} = \gamma_{s1} + \gamma_{s2} - \beta_{s1/s2}, \quad (3)$$

where γ_{s1} and γ_{s2} are surface energies of the respective slabs forming the interface, and $\beta_{s1/s2}$ the adhesion energy defined earlier.

The planar and macroscopic averaged potentials as well as the charge density differences were computed using the VASPKIT post-processing code¹⁰⁶. Graphical drawings were produced using VESTA¹⁰⁷ and OVITO¹⁰⁸.

The vertical ionization potential (IP) is calculated using a bulk-based definition, via the electrostatic alignment between the surface and the bulk as follows¹⁰⁹:

$$\varepsilon_{IP} = \Delta\varepsilon_{\text{vac-ref}} - \Delta\varepsilon_{\text{VBM-ref}}$$

where $\Delta\varepsilon_{\text{vac-ref}}$ is the difference between the electrostatic potential in the vacuum region and the bulk-like reference level in the slab (the 1s states of Cu and Ti in the middle of the Cu₂O(111) and TiO₂(101) slabs, respectively). The second term, $\Delta\varepsilon_{\text{VBM-ref}}$, is the difference in eigenvalue energy between the valence band maximum (VBM) and reference level from bulk calculations. The electron affinity (EA) is obtained by subtracting the obtained band gap value from the ionization potential.

The macroscopic average of the electrostatic potential along the non-periodic direction of the interfaces was computed using the MacroDensity package¹¹⁰.

The heterostructures with different degrees of lattice mismatch (strain) were generated using the QuantumATK software developed by Synopsys¹¹¹ which provides a user-friendly setting to adjust the lattice vectors and align the crystal structures to create the desired heterostructures. In generating the interfaces, Cu₂O was subjected to strain (treated as a film), a consequence of its deposition as the top layer in the Cu₂O/TiO₂ fabrication process¹¹²⁻¹¹⁴.

Results and Discussion

The surfaces. Determining suitable surface orientations for the construction of a heterostructure poses a challenge due to its impact on band bending characteristics. This challenge arises from the involvement of surface dipoles in the determination of the VB and CB edges, which are critical factors in establishing interfacial band alignment. These band positions are intrinsically influenced by the surface orientation, composition, atomistic and electronic structure, all of which collectively contribute to the surface dipole effects¹¹⁵⁻¹¹⁸. From a computational standpoint, a key constraint in selecting the right surfaces is the assessment of surface polarity, as polar surfaces inherently exhibit a notable electrostatic instability¹¹⁹. This instability arises from the presence of macroscopic dipoles oriented perpendicular to the surface within each unit cell that accumulate, necessitating

the introduction of compensating charges to neutralize these dipoles. Achieving such compensation in practice involves extensive surface modifications, including significant adjustments in stoichiometry, faceting, spontaneous desorption of atoms, large-cell reconstruction due to the ordering of surface vacancies, among other complex processes^{120, 121}.

Experimentally, the primary surfaces in heterostructures are identified through high-resolution TEM analysis. This method unveils predominant lattice spacings, facilitating the determination of the corresponding surfaces for each constituent material within the heterostructure. In the specific case of the Cu₂O/TiO₂ heterojunction, surfaces (111) and (101) have consistently emerged as the dominant surfaces for Cu₂O and TiO₂, respectively, across diverse morphologies and fabrication techniques^{37, 43, 54, 102-104}. Notably, these surfaces exhibit non-polar characteristics, showing no electrostatic instabilities. Therefore, in the current study, surfaces (111) and (101) are selected for Cu₂O and TiO₂, respectively.

The initial geometry of the slabs for a 4-bilayer TiO₂ and 6-trilayer Cu₂O are shown in **Figure S1**. The thickness of the surfaces has been optimized with respect to the surface energy (**Equation 1**). The results using PBE functional are presented in **Figure S2** which indicate that the surface energy quickly converged to a value of 1.13 J/m² for a 4-bilayer TiO₂ and 0.77 J/m² for a 6-trilayer Cu₂O, in agreement with the earlier studies^{122, 123}.

Interfaces.

Geometry. To construct the interfaces, we have confined this study to epitaxial heterostructures, with lattice mismatch values predominantly confined within a 10% threshold^{124, 125}. It is well-established that an escalated degree of lattice mismatch can lead to the formation of defects in the heterostructure, such as dislocations, threading dislocations, misfit dislocations, and cracks¹²⁶. Severe lattice mismatch will cause dislocations at the interface and results in electrical defects such

as interface traps¹²⁷. These defects can significantly degrade the electronic and optical properties of the heterostructure, which can limit their practical applications. **Figure 1** shows a map of all the possible heterostructure of Cu₂O(111)/TiO₂(101) as a function of the mean absolute strain (lattice mismatch) –which is defined as $\frac{a_{\text{TiO}_2} - a_{\text{Cu}_2\text{O}}}{a_{\text{TiO}_2}}$, where a is lattice constant– and number of atoms in the unit cell of the heterostructures.

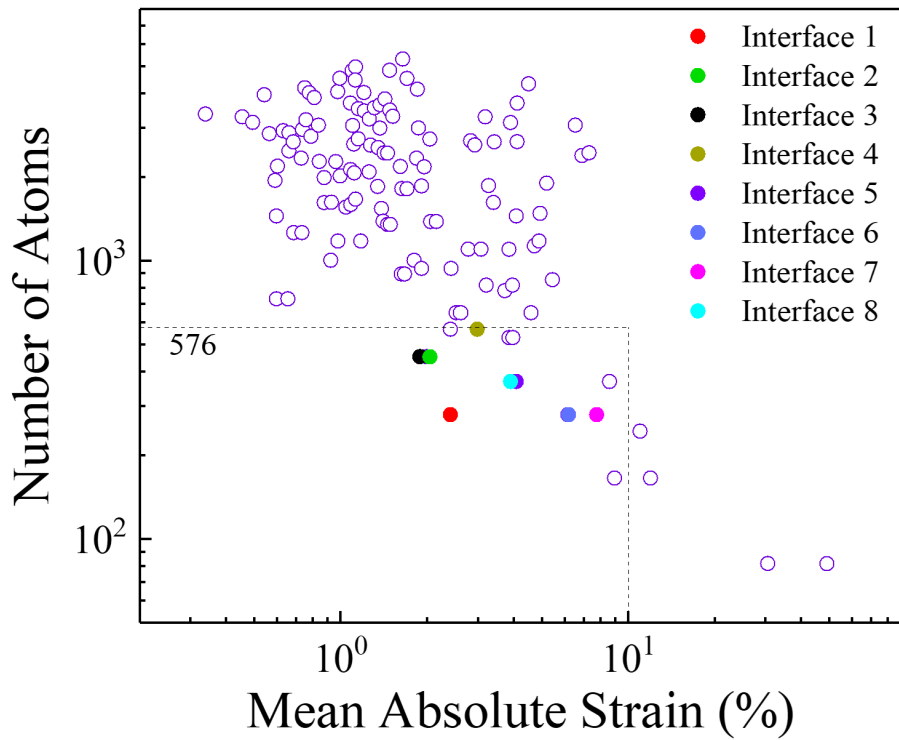


Figure 1. Map of all the possible heterostructures of Cu₂O(111)/TiO₂(101) as a function of lattice mismatch (as defined in the text), and total number of atoms in the unit cell. The eight selected interfaces, confined within 576-atom limit, and 10% mean absolute strain, are highlighted in different colors.

In the current study, a systematic approach was employed to select the interfaces, ensuring that the strain remained within a limit of 10%, while also maintain computational feasibility (total number of atoms ≤ 576). As shown in **Figure 1**, this criterion resulted in eight distinct interfaces for subsequent analysis. A detailed numerical analysis of the strain present at the selected interfaces is outlined in **Table 1**.

Table 1. Details of the strain matrices in the supercell of the selected interfaces and corresponding adhesive and interface energies, where ϵ_{xx} and ϵ_{yy} are the normal strains along the x and y directions and ϵ_{xy} represents the shear strain in the x-y plane.

Interface	$\epsilon_{xx}(\%)$	$\epsilon_{yy}(\%)$	$\epsilon_{xy}(\%)$	Mean absolute strain (%)	Adhesive en. β (J/m ²)	Interface en. γ (J/m ²)
1	5.87	-1.39	0.00	2.42	2.29	-0.13
2	4.59	-1.39	0.00	2.03	2.94	-0.95
3	3.12	0.01	-2.55	1.89	1.41	0.48
4	-5.15	-2.14	-1.66	2.98	2.03	0.04
5	-5.13	4.36	-2.74	4.07	1.48	0.53
6	-9.02	2.02	7.52	6.19	1.90	1.16
7	-14.60	8.69	0.00	7.76	1.43	1.82
8	5.05	-5.76	-0.88	3.90	1.27	0.48

From the geometrical standpoint, the main connecting point between the two materials are the outermost oxygen atoms, which is a standard bridging mechanism for metal oxides. On the TiO₂(101) surface, there are the undercoordinated topmost surface O atoms and subsurface Ti atoms, while on the Cu₂O(111) surface there are subsurface undercoordinated Cu atoms present in the same plane with coordinatively saturated Cu atoms linking two O atoms, while the topmost surface O atoms undercoordinated. However, due to the approximately 2:1 ratio of available Ti to Cu atoms (per unit cell or comparable surface area) as well as $O_{TiO_2}^{top}$ to $O_{Cu_2O}^{top}$ atoms, it is to be expected that a certain number of bonds will remain undercoordinated.

Upon relaxation, the TiO₂ topmost 2-fold coordinated O atoms formed a bond at the interface with the singly coordinated Cu atoms on the Cu₂O side and the 3-fold coordinated O atoms from the Cu₂O side bonded with the 5-fold undercoordinated titanium atoms from TiO₂. However, depending on the amount of lateral and shear strain present in the initial model, the

number of formed bonds differs greatly amongst the eight chosen interfaces. This can be observed in the calculated adhesive energy, listed in **Table 1**, which is a direct quantity (at the computational level) allowing one to evaluate the probability of observing the corresponding epitaxial interface. From the computed values, it is notable that not all interfacial structures result in an equal energy gain once the interface is formed.

The energetically most stable interface is found to be interface 2, which is shown in **Figure 2**. This interface has the lowest amount of lateral strain (present in the film), while at the same time undergoing no shear strain. In this configuration, all the O atoms from the substrate and film are coordinatively saturated upon relaxation (completion of their octet), while every other Ti atom remains undercoordinated.

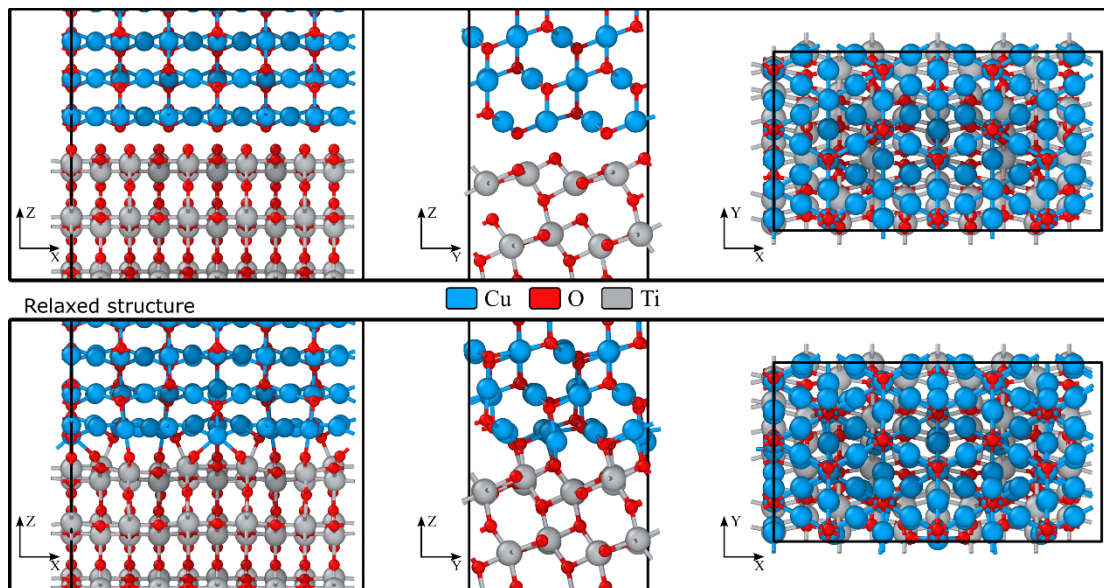


Figure 2. Initial and relaxed atomic structure of the most stable $\text{Cu}_2\text{O}/\text{TiO}_2$ interface 2, viewed along all three crystallographic axes. Vacuum is present along the Z-axis but is omitted for clarity.

The accurate assessment of band bending properties at interfaces requires a comprehensive understanding of the structural and electronic changes induced by the formation of the interface. The independent slab approximation only provides an incomplete representation of the band alignment, resulting in significant discrepancies when compared to experimental data¹²⁸. Explicit

interfacial relaxations can induce a shift in the band alignment as much as 130 meV highlighting the key role of the relaxation in the precise estimation of band alignment¹²⁹. The relaxed structures of interfaces 1-8 are shown in **Figure S3**.

Band alignment. When two semiconductor materials form an interface, a discontinuity in their band edges occurs. In the computational evaluation of these relative band edges, a challenge arises due to the absence of an absolute reference energy in an infinite solid attributed to the long-range nature of the columbic interaction^{130, 131}. To address this, the average electrostatic potential has been suggested as a consistent energy reference in such systems¹³²⁻¹³⁴. The method involves first determining the average of the electrostatic potential of the interface, followed by calculating the band edges of the individual slabs relative to their average electrostatic potential for the individual slabs. It is crucial to account for the strain induced by interfacial relaxations; therefore, the relaxed slab geometries should be utilized in these calculations without further relaxations⁴⁸.

Functional. Within the framework of DFT, generalized gradient approximation (GGA) functionals suffer from self-interaction errors which result in the systematic underestimation of band gaps and the overestimation of cohesive energies in materials¹³⁵. To address these limitations, hybrid functionals, which integrate a mix of Fock exchange with semilocal exchange, are designed to mitigate this delocalization error¹³⁶. The partial incorporation of the exact exchange from Hartree-Fock theory into these functionals helps to correct the self-interaction error, thereby providing a more accurate representation of electron correlation and localization. This adjustment is crucial for electronic properties as it leads to a more precise prediction of band gaps. However, hybrid functionals are computationally demanding and the relaxation of the heterostructures comprising hundreds of atoms becomes impractical. Consequently, a synergic approach that combines the computational efficiency of GGA functionals with the accuracy of hybrid functionals

can be employed. This combined approach enables an accurate assessment of the band bending, at a reasonable computational cost. It consists of heterostructure relaxation via GGA functionals and assessment of band edge positions of isolated slabs via hybrid functionals.

In calculating the band alignment, since the average electrostatic potential is a function of the ground state charge density, and the difference in the distribution of electronic density obtained with different functionals which determines the Hartree potential, is small^{137, 138}, the potential lineup can be accurately determined via GGA^{129, 135, 139-141} and many-body corrections^{142, 143} or hybrid functionals such as PBE0 schemes¹²⁹ can barely affect the band potential lineup in accordance with findings for semiconductor-insulator interfaces^{135, 141}. For instance, it has been shown that the potential alignments calculated within the GGA are in agreement with those calculated using HSE to within 50 meV, despite the GGA calculations being 10–100 times less computationally expensive¹³⁸. In other hybrid functional study of Si and TiO₂ surfaces¹⁴⁴ and a self-consistent GW study of an Si/SiO₂ interface¹³⁵ have indeed shown that the changes in the averaged electrostatic potential from the semilocal values are less than 0.1 eV at these surfaces and interface. Moreover, the functional dependence of the formation energies of Si self-interstitials as a function of the electronic chemical potential has shown that taking the average electrostatic potential as the reference of the energy results in invariant features in the formation energy for any given value of chemical potential¹³⁷. Thus, considering the accuracy of potential alignments via GGA, they can be combined with hybrid calculations of the isolated slabs' band structure toward accurate band alignments with a high computational efficiency¹³⁸.

While GGA calculations present a lower computational cost compared to more sophisticated methods, the computational demands still escalate significantly for large-scale systems. Therefore, it is imperative to employ the minimal slab thicknesses and thus lowest

possible number of atoms in the calculations. This reduction in system size is justified by the localized nature of interfacial electronic properties at neutral interfaces¹³⁹. The interfacial properties are usually confined within a few atomic units from the interface beyond where the bulk properties of charge density rapidly converge. To consider the smallest possible interface and verify the assessment of the slab thicknesses via surface energy (**Figure S2**), the average electrostatic potential of interface 1 is calculated in comparison to the independent slabs' approximation in **Figure 3**. Since TiO₂ is the substrate and does not undergo strain (only chemical alterations at the interface itself), its electrostatic potential, as shown in **Figure 3a**, remains relatively unchanged when compared with the explicit interfaces depicted in **Figure 3c** and **3d**. In contrast, due to the imposed strain on Cu₂O, it is more influenced by the interfacial effects which only penetrate no more than two atomic layers from the interface as can be seen in **Figure 3c**. To validate the sufficiency of the 6-layer Cu₂O slab, an 8-layer slab is also examined in **Figure 3d** which reveals a continuation of the bulk-like behavior within the central layers of the slab. This finding suggests that the 6-layer Cu₂O slab adequately captures the intrinsic electrostatic characteristics of the bulk. Consequently, Cu₂O(6-layer)/TiO₂ (4-layer) model configuration is selected throughout this study.

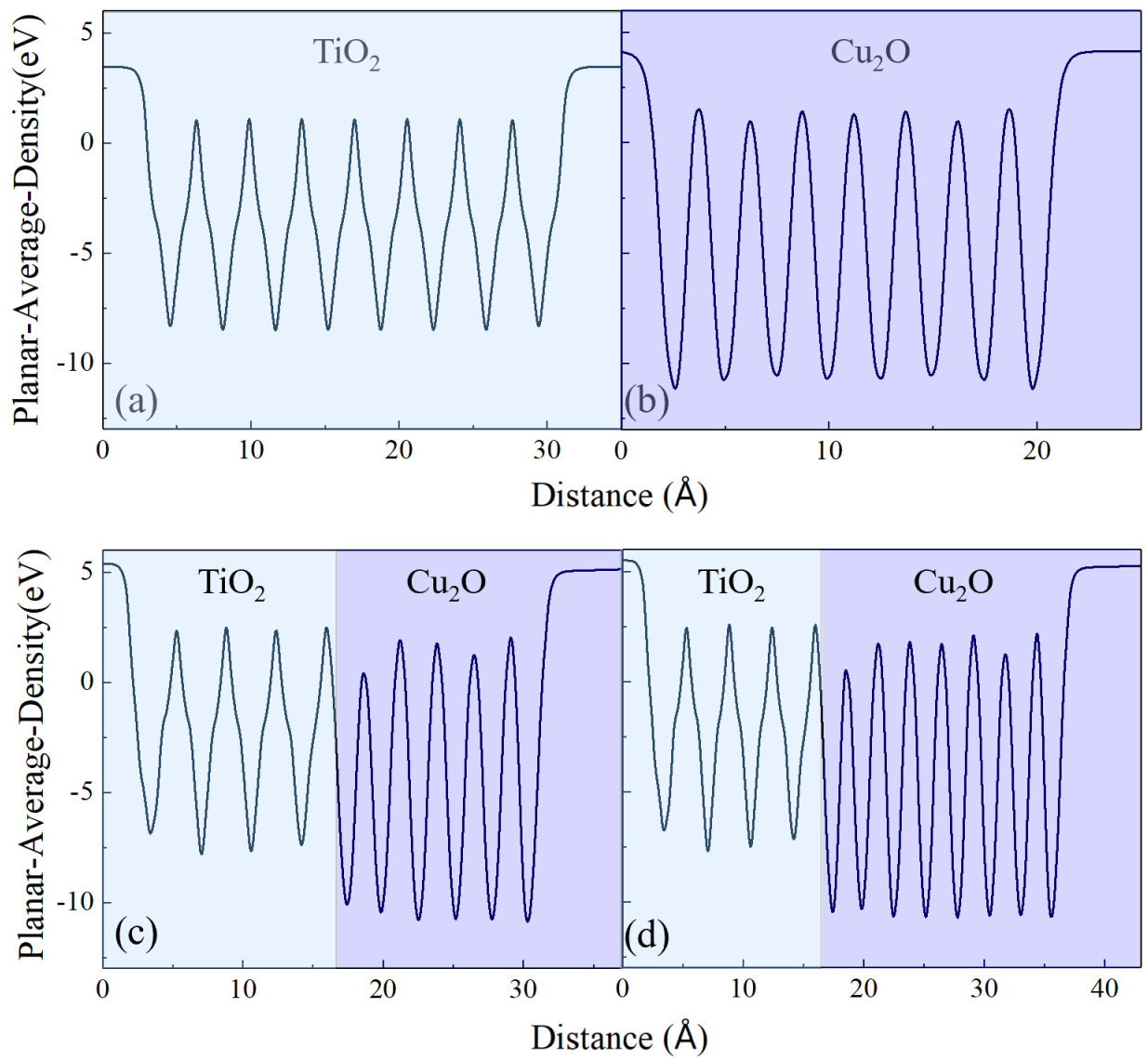


Figure 3. Thickness assessment of interface 1 in relation to the thickness of the Cu₂O through planer-averaged electrostatic potential: (a,b) independent slab approximation (before contact). (c) explicit interface of Cu₂O/TiO₂ with 6 layers of Cu₂O, and (d) 8 layers of Cu₂O.

As aforementioned, an electrostatic potential approach has been employed to assess the band bending of the various interfaces. This method entails calculating the electrostatic potential, averaged across the x-y plane. The resulting data for interface 2 is depicted in **Figure 4**, where the planar-averaged electrostatic potential is plotted as a function of the distance along the z-axis, normal to the interface plane. Notably, this profile shows distinct minima corresponding to atomic planes, indicating areas with higher electron density. In the section of the interface composed of TiO₂ **Figure 4a**, notable deviations are observed in the potential profile. These deviations are attributed to the displacement of O atoms relative to Ti-containing planes, a structural feature inherent to the anatase phase of TiO₂. This atomic arrangement results in characteristic ‘shoulders’ in the potential curve, observable throughout the entire extent of the anatase layer.

When determining an appropriate reference point on the electrostatic potential curve, concerns arise regarding the precision of planar-averaged potentials at planes containing atoms. The main challenge comes from the necessity to integrate the electrostatic potential in proximity to atomic positions, where the potential changes very quickly and sharply. These steep variations in potential make it difficult to compute the potential accurately, particularly over confined regions such as within a single lattice period. To address this issue, as outlined by Conesa¹³⁴, in this study, instead of relying on the planar-averaged potential at the atom-containing planes, we utilized the energy value at the point of zero slope (termed E_{top}). These zero-slope points typically occur near the midpoint between successive atomic planes. This method is considered more reliable for determining the reference value for electronic levels. The analysis reveals that these zero slope values display oscillations within each slab near the interface, but they stabilize to a constant value towards the center of each slab. The resultant values for interface 2 are $E_{\text{top}} = 2.11$ eV and 1.79 eV for the TiO₂ and Cu₂O regions, respectively.

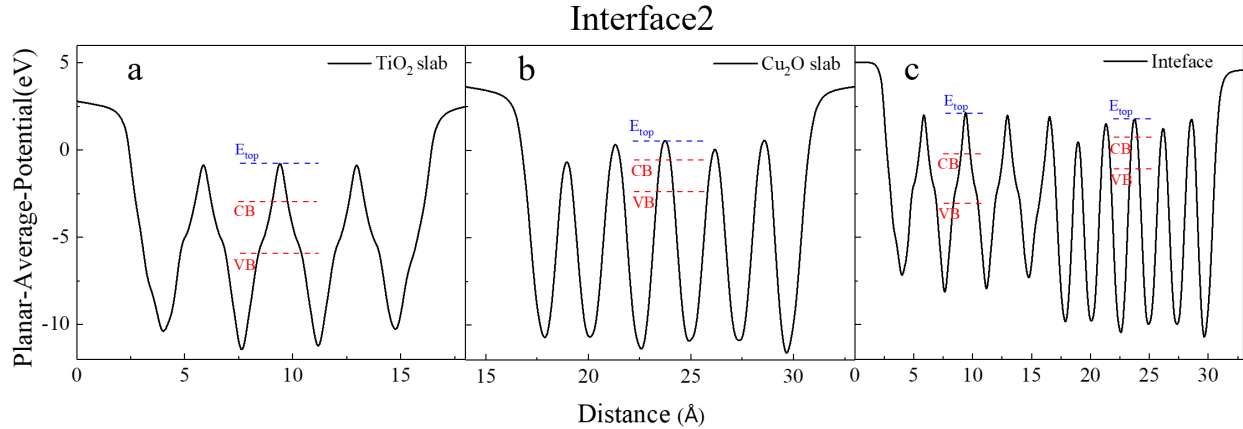


Figure 4. Planar-averaged electrostatic potentials in the x - y plane of (a,b) the isolated slabs with the interface geometries, and (c) of interface 2 as a function of the distance along the z -direction, normal to the interface. E_{top} denotes the reference energy, and the CB and VB edges in the interface are aligned based on their respective values to the E_{top} in the isolated slabs' calculations.

After establishing the reference energies (E_{top}), the next step is determining the band edges of the individual slabs relative to these reference energies. To achieve this, the planar-averaged electrostatic potential was computed for the individual TiO_2 and Cu_2O slabs. However, it is important to note that the slabs acting as films are distorted due to epitaxial strain and to accurately represent the electronic properties under these conditions, it is imperative to calculate the electrostatic potentials for the distorted structures. Thus, hybrid functional calculations were performed, considering the distorted slab structures as they exist at the interface without any further relaxations. **Figure 4a,b** show the results of the hybrid calculation for the individual TiO_2 and Cu_2O , respectively where the relative positions of the VB and CB edges are shown with respect to the E_{top} for each slab. With the band edges of both materials positioned relative to the reference energy, the final band offsets are conclusively determined and depicted in **Figure 4c**. The findings suggest a staggered-type alignment at the interface wherein the band edges of Cu_2O are positioned at a higher energy level compared to those of TiO_2 . Similar results are obtained for the other interfaces and the details are presented in **Figures S4-10**. The band alignment results for all the interfaces are summarized in **Figure 4**. This figure highlights the variations in the positions of the

VB and CB edges across different interfaces as a result of their different interfacial morphologies. Despite these variations, a key observation is the consistent presence of a staggered-type alignment across all the interfaces. The values of the band offsets as noted in the graph, are comparable to the experimental values of $\Delta E_v = 1.93$ eV¹⁴⁵, 1.71 eV¹⁴⁶, $\Delta E_c = 0.81$ eV¹⁴⁵, 0.88 eV¹⁴⁶. This uniformity in the alignment type, despite differences in the specific energy levels of the band edges, underscores a fundamental characteristic of these heterojunctions.

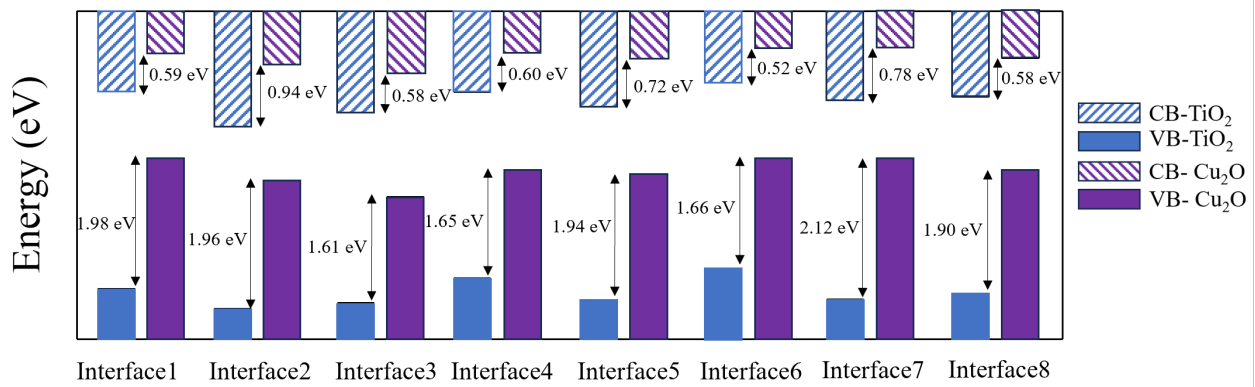


Figure 5. Summary of the band alignment results for interfaces 1-8. The band offsets, ΔE_v and ΔE_c , are indicated for each interface.

For comparison, we computed the valence and conduction band offsets in the independent compound approximation and through the averaged electrostatic potential method (results listed in **Table S1** and **Table S2**). The computed ionization potential (IP) and electron affinity (EA) of TiO₂ and Cu₂O compare well with experimental values, however, the band offsets are overestimated in this approach. When employing the macroscopic averaging technique of the interface electrostatic potential to obtain the offset in the potential across the interface, the results (1.93 eV for VBO and 0.42 eV for CBO) compare much closer to the measured experimental values. This confirms once again how indispensable explicit modelling of interfacial structures is for accurate electronic band behavior at junctions.

While band alignment configurations provide valuable insights into the arrangement of band edges at the interface, they do not conclusively establish the charge transfer properties. Specifically, as illustrated in **Figure 6**, within a staggered-type alignment between two semiconductors (SC1 and SC2), there exist two possible configurations for charge transfer. **Figure 6a** depicts a type II configuration, wherein charge separation is achieved via the antiparallel transfer of photoexcited electrons and holes. in the opposite direction. Whereas **Figure 6b** depicts a scenario were the photoexcited electrons in SC2 recombine with the holes in SC1 through a Z-scheme mechanism.

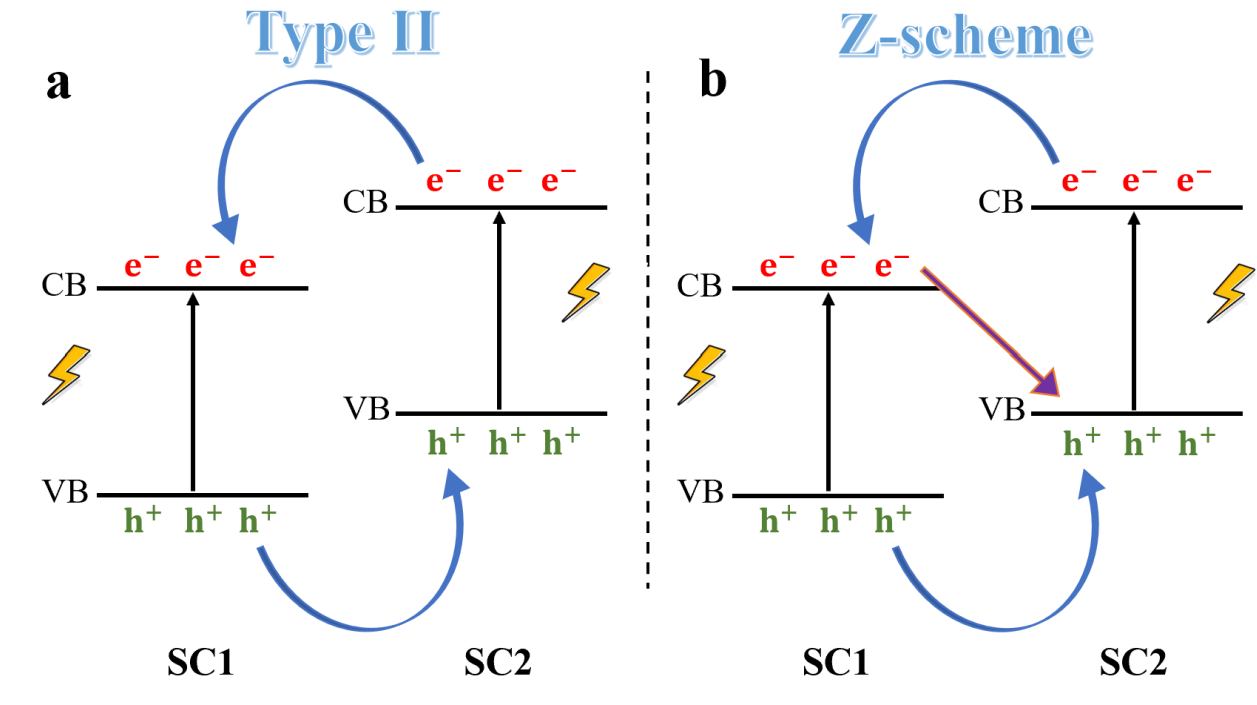


Figure 6. Schematic illustration of charge transfer mechanism after light illumination. (a) type II where electrons and holes transfer in an antiparallel way, and (b) Z-scheme where after the antiparallel charge transfer, electrons in SC1 combine with the holes in SC2 (SC stands for semiconductor).

Hence, to differentiate between a type II and Z-scheme charge transfer mechanisms, it is essential to quantify the charge density difference at the interfaces, defines as

$$\Delta\rho = \rho_{interface} - \rho_{TiO_2} - \rho_{Cu_2O}, \quad (2)$$

where $\Delta\rho$ is the charge density difference at the interface, $\rho_{interface}$ is the charge density of the interface, and ρ_{TiO_2} and ρ_{Cu_2O} are the charge densities of the corresponding slabs before contact.

Figure 7 shows $\Delta\rho$ for interface 2 where the dashed line represents the midpoint layer of the interface. The figure suggests a directional charge transfer towards the interface from both the Cu_2O and TiO_2 layers. However, a closer inspection of the structure reveals that the electrons are transferred from the transition metal towards the oxygen. That is nothing else than the bond formation process confirmed which was discussed when the adhesion energies were discussed. The two charge depletion regions in **Figure 7** are approximately half the value of the main charge accumulation region at the interface. In addition, we computed the electron dipole moment at the interface. A maximal value of 0.1 D was obtained, arising from the disparity between the number of metal ions present to form bonds at the interface (see discussion on structure at the interface), which offers space for band bending to occur.

The charge density difference for all other interfaces is presented in **Figures. S11-17**. A consistent pattern of charge transfer between the transition metal and the interface oxygen is found across all interfaces. However, one should treat these results with care as they have been computed with a semi-local functional, thus not entirely circumventing the well-known charge delocalization error for *d*-electron bearing transition metals, which can affect the value of the interface dipole and corresponding charge transfer.

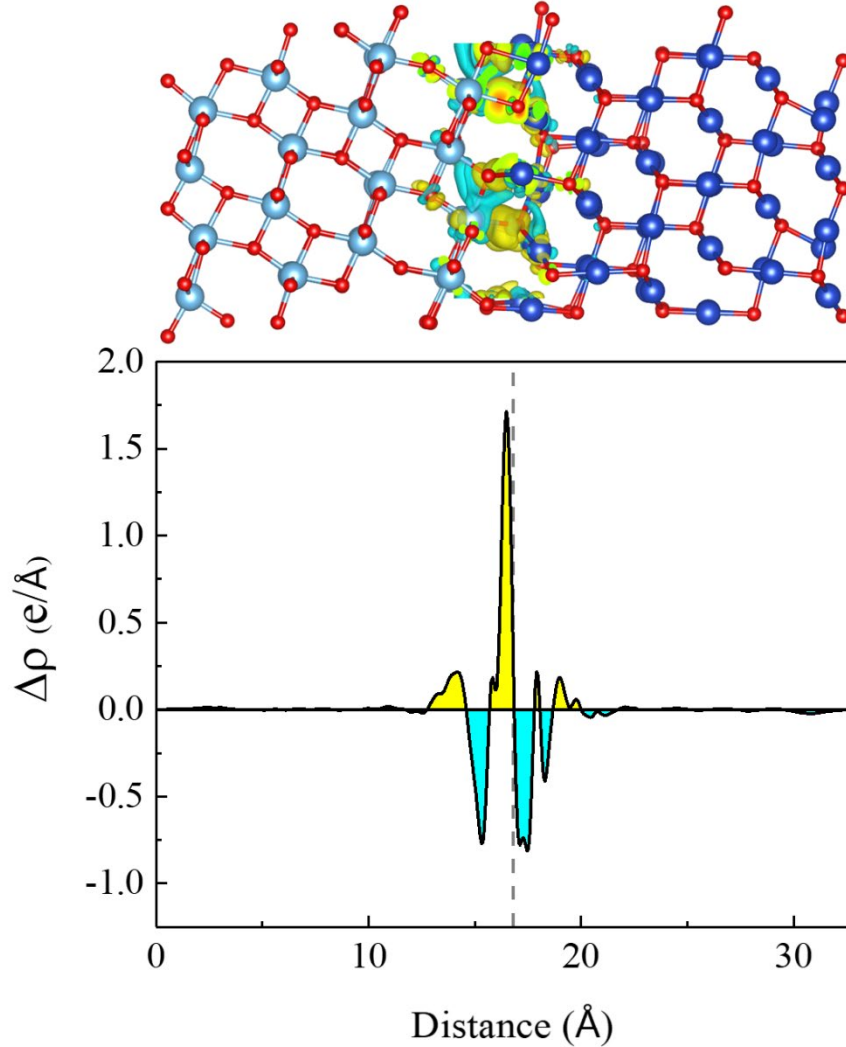


Figure 7. Charge density difference of interface 2. Yellow: charge accumulation. Cyan: charge depletion. The dashed line represents the midpoint layer of the interface. Isosurface value is set to 0.0015 for the orbital visualization.

To further verify the charge transfer direction, fermi energies (E_F) are evaluated before and after contact. When two semiconductors with different fermi energies come into contact, charge transfer occurs from the material with the higher E_F to the one with the lower E_F until the fermi levels equilibrate. **Figure 8c** shows the E_F of interface 2 in comparison with the E_F of the individual slabs before contact (**Figure 8a,b**). It is evident that Cu_2O has a higher E_F compared to TiO_2 . Consequently, upon contact in the interface, charges transfer from Cu_2O to TiO_2 until the

fermi levels reach equilibrium. This charge transfer direction is consistent with the charge depletion observed in Cu_2O and charge accumulation in TiO_2 , as seen in **Figure 7**. The fermi energy assessment for other interfaces is shown in **Figures. S18-24**. The findings suggest the same charge transfer mechanism across all the interfaces.

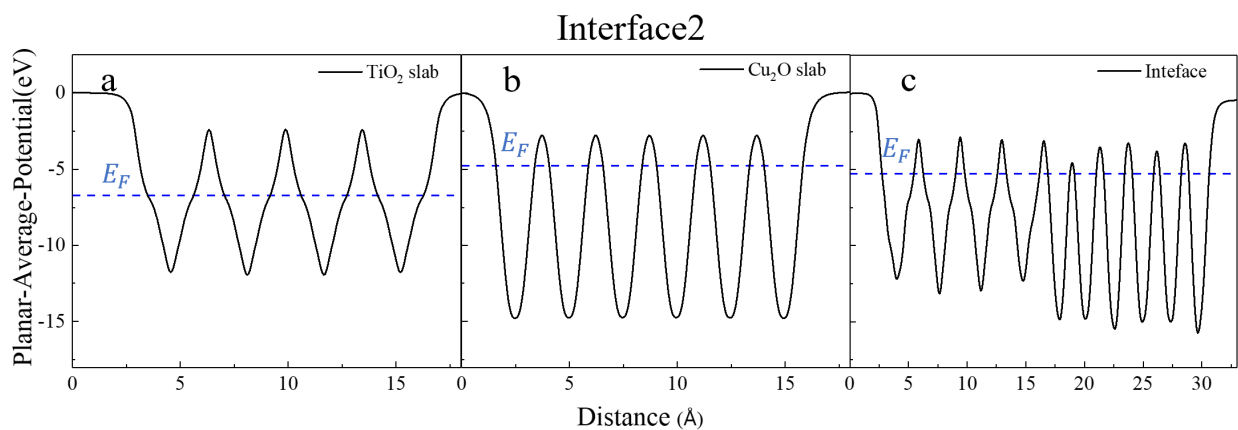


Figure 8. Fermi energy assessment of interface 2 (a,b) before and (c) after contact

The comprehensive analysis of charge transfer mechanisms in **Figure 4, 5, 7, and 8**, leads to the proposal of distinct behavior under visible and ultraviolet light illumination, specifically focusing on the photocatalytic behavior of the $\text{Cu}_2\text{O}/\text{TiO}_2$ interface. As shown in **Figure 9a**, under visible light, only Cu_2O would be photoexcited due to its suitable band gap. This could potentially result in the generation of photoexcited electrons and holes within Cu_2O . However, the band bending configuration at the interface, given the charge depletion and accumulation in Cu_2O and TiO_2 , respectively, causes the Cu_2O bands to bend upward and TiO_2 to bend downward, forming a Z-scheme band bending configuration. In this configuration, the photoexcited electrons in Cu_2O would encounter an energy barrier that hinders their transfer to TiO_2 . Consequently, these photoexcited electrons and holes are unable to separate efficiently, leading to their recombination within the Cu_2O material. This recombination typically occurs on a very fast timescale (femtosecond to picosecond), which is much quicker than the timescale of chemical reactions

(milliseconds)¹⁴⁷. As a result, these carriers recombine before they can participate in photocatalytic reactions, leading to reduced photocatalytic activity under visible light.

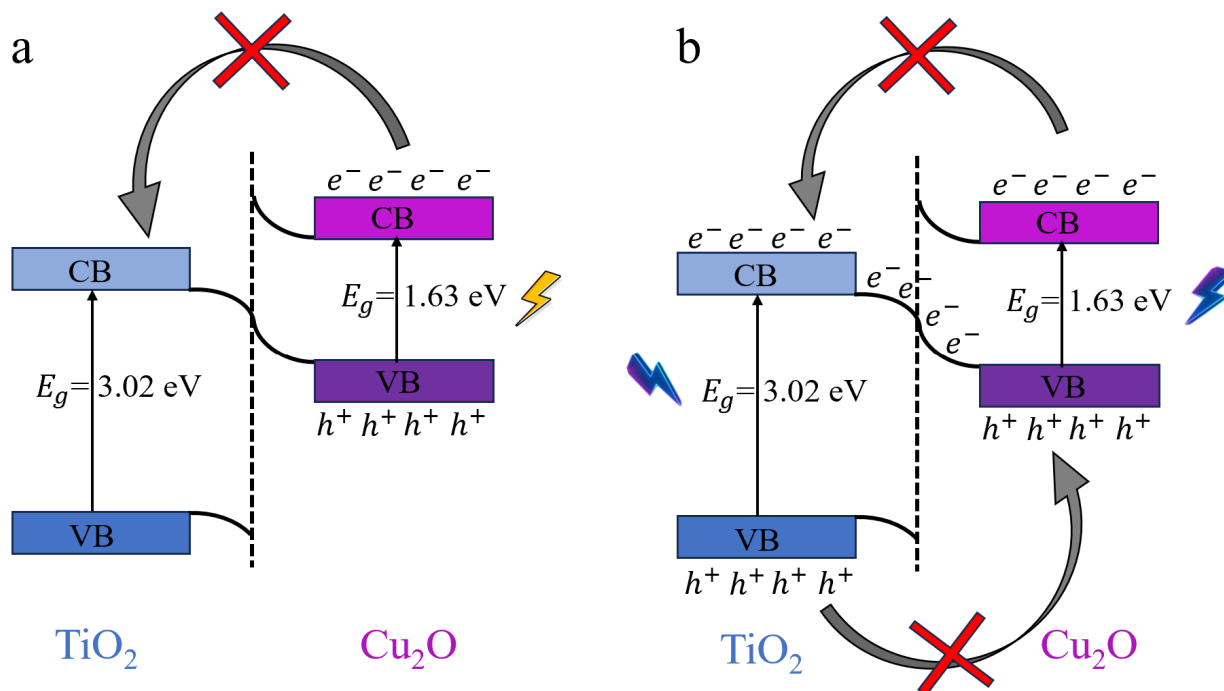


Figure 9. The proposed band bending configuration for $\text{Cu}_2\text{O}/\text{TiO}_2$ interfaces under a) visible and b) ultraviolet light illumination.

In contrast, under ultraviolet or violet light illumination, both Cu_2O and TiO_2 are excited. In this scenario, the Z-scheme band bending plays a pivotal role in dictating the charge transfer dynamics. Specifically, the photoexcited electrons from TiO_2 recombine with the photoexcited holes in Cu_2O . This recombination process effectively separates the photoexcited holes in TiO_2 from the photoexcited electrons in Cu_2O . The separated charge carriers – photoexcited holes on TiO_2 and photoexcited electrons on Cu_2O – are now available to participate in photocatalytic chemical reactions. This separation enhances the photocatalytic efficiency under ultraviolet light, as the carriers are able to participate in redox reactions. This observed Z-scheme band alignment configuration is consistent with numerous experimental investigations that have analyzed similar crystal facets, specifically $\text{TiO}_2(101)$ and $\text{Cu}_2\text{O}(111)$ ^{78, 114, 148-151}.

Conclusion

In conclusion, this study delves into the intricate interplay between interfacial morphologies, band bending effects, and charge transfer dynamics in anatase $\text{Cu}_2\text{O}/\text{TiO}_2$ epitaxial heterostructures for photocatalytic applications. Through a systematic exploration, starting from well-defined TiO_2 (101) and Cu_2O (111) slab structures, explicit epitaxial heterojunctions where TiO_2 serves as a substrate for a Cu_2O film were created. Out of the obtained structures, those with a lattice mismatch of less than 10% were selected for further optimization. Eight distinct interfaces were identified, all with a consistent staggered-type band alignment, providing valuable insights into the fundamental characteristics of these heterojunctions.

Despite variations in band edge positions, a systematic charge transfer from Cu_2O to TiO_2 was observed across all interfaces. The proposed band bending can help explain the nuances of charge separation at the $\text{Cu}_2\text{O}/\text{TiO}_2$ interface evidenced in earlier experiments. The observed Z-scheme band alignment under ultraviolet light aligns with experimental investigations, highlighting its relevance to enhancing photocatalytic efficiency. This theoretical investigation contributes to the understanding of the structural and electronic factors influencing the photocatalytic behavior of heterostructures, paving the way for the rational design and optimization of photocatalytic materials for environmental remediation applications.

It is essential to recognize that the experimental processes inherently introduce defects and impurities which can significantly influence the band bending properties of interfaces. Future research should therefore be directed towards a detailed investigation of how these unavoidable imperfections affect the electronic structure of the interfaces. This entails a systematic study of the type and concentrations of defects and impurities, as well as their spatial distribution within the material. Additionally, it is crucial to explore the mechanisms through which these defects and

impurities interact with materials' electronic states. Such studies are vital for advancing our theoretical understanding of the interfaces as well as providing directions for experimental studies.

Acknowledgments

A. Ž. and N. H. d. L. acknowledge the NWO ECHO grant (712.018.005) for funding.

References

- (1) Yan, J.; Wu, H.; Chen, H.; Zhang, Y.; Zhang, F.; Liu, S. F. Fabrication of TiO₂/C₃N₄ heterostructure for enhanced photocatalytic Z-scheme overall water splitting. *Applied Catalysis B: Environmental* **2016**, *191*, 130-137. DOI: <https://doi.org/10.1016/j.apcatb.2016.03.026>.
- (2) Jeon, N. J.; Noh, J. H.; Kim, Y. C.; Yang, W. S.; Ryu, S.; Seok, S. I. Solvent engineering for high-performance inorganic–organic hybrid perovskite solar cells. *Nat. Mater.* **2014**, *13* (9), 897-903.
- (3) Kim, H.-S.; Lee, C.-R.; Im, J.-H.; Lee, K.-B.; Moehl, T.; Marchioro, A.; Moon, S.-J.; Humphry-Baker, R.; Yum, J.-H.; Moser, J. E. Lead iodide perovskite sensitized all-solid-state submicron thin film mesoscopic solar cell with efficiency exceeding 9%. *Scientific reports* **2012**, *2* (1), 591.
- (4) Malinkiewicz, O.; Yella, A.; Lee, Y.; Espallargas, G.; Graetzel, M.; Nazeeruddin, M.; Bolink, H. *Nat. Photonics* **8** (2), 128–132 (2014). 2013.
- (5) Huang, J.; Yuan, Y.; Shao, Y.; Yan, Y. Understanding the physical properties of hybrid perovskites for photovoltaic applications. *Nature Reviews Materials* **2017**, *2* (7), 1-19.
- (6) Dong, S.; Feng, J.; Fan, M.; Pi, Y.; Hu, L.; Han, X.; Liu, M.; Sun, J.; Sun, J. Recent developments in heterogeneous photocatalytic water treatment using visible light-responsive photocatalysts: a review. *RSC Advances* **2015**, *5* (19), 14610-14630, 10.1039/C4RA13734E. DOI: 10.1039/C4RA13734E.
- (7) Tian, J.; Zhao, Z.; Kumar, A.; Boughton, R. I.; Liu, H. Recent progress in design, synthesis, and applications of one-dimensional TiO₂ nanostructured surface heterostructures: a review. *Chemical Society Reviews* **2014**, *43* (20), 6920-6937, 10.1039/C4CS00180J. DOI: 10.1039/C4CS00180J.
- (8) Li, A.; Wang, Z.; Yin, H.; Wang, S.; Yan, P.; Huang, B.; Wang, X.; Li, R.; Zong, X.; Han, H.; Li, C. Understanding the anatase–rutile phase junction in charge separation and transfer in a TiO₂ electrode for photoelectrochemical water splitting. *Chem. Sci.* **2016**, *7* (9), 6076-6082, 10.1039/C6SC01611A. DOI: 10.1039/C6SC01611A.
- (9) Li, H.; Yu, H.; Quan, X.; Chen, S.; Zhao, H. Improved Photocatalytic Performance of Heterojunction by Controlling the Contact Facet: High Electron Transfer Capacity between TiO₂ and the {110} Facet of BiVO₄ Caused by Suitable Energy Band Alignment. *Advanced Functional Materials* **2015**, *25* (20), 3074-3080. DOI: <https://doi.org/10.1002/adfm.201500521> (accessed 2023/10/24).
- (10) Zhang, Z.; Yates Jr, J. T. Band bending in semiconductors: chemical and physical consequences at surfaces and interfaces. *Chemical reviews* **2012**, *112* (10), 5520-5551.
- (11) Ihn, T. *Semiconductor Nanostructures: Quantum states and electronic transport*; Oxford University Press, 2009. DOI: 10.1093/acprof:oso/9780199534425.001.0001.
- (12) Huang, M. H.; Madasu, M. Facet-dependent and interfacial plane-related photocatalytic behaviors of semiconductor nanocrystals and heterostructures. *Nano Today* **2019**, *28*, 100768. DOI: <https://doi.org/10.1016/j.nantod.2019.100768>.
- (13) Kubyshkina, E.; Unge, M. Impact of interfacial structure on the charge dynamics in nanocomposite dielectrics. *Journal of Applied Physics* **2019**, *125* (4). DOI: 10.1063/1.5078800 (accessed 12/20/2023).
- (14) Mora-Fonz, D.; Buckeridge, J.; Logsdail, A. J.; Scanlon, D. O.; Sokol, A. A.; Woodley, S.; Catlow, C. R. A. Morphological Features and Band Bending at Nonpolar Surfaces of ZnO. *The Journal of Physical Chemistry C* **2015**, *119* (21), 11598-11611. DOI: 10.1021/acs.jpcc.5b01331.

- (15) Zhang, Z.; Yates, J. T., Jr. Band Bending in Semiconductors: Chemical and Physical Consequences at Surfaces and Interfaces. *Chemical Reviews* **2012**, *112* (10), 5520-5551. DOI: 10.1021/cr3000626.
- (16) Ramana, C. V.; Makeswaran, N.; Zade, V.; Das, D.; Tan, S.; Xu, S.; Beyerlein, I. J. Fabrication and Characterization of High-Quality Epitaxial Nanocolumnar Niobium Films with Abrupt Interfaces on YSZ(001). *The Journal of Physical Chemistry C* **2022**, *126* (4), 2098-2107. DOI: 10.1021/acs.jpcc.1c08738.
- (17) Bao, T.; Wang, J.; Liu, C. Recent advances in epitaxial heterostructures for electrochemical applications. *Nanoscale Adv* **2023**, *5* (2), 313-322. DOI: 10.1039/d2na00710j From NLM.
- (18) Ohtake, A.; Yang, X. Fabrication of Lattice-Mismatched MoTe₂/MoSe₂ Heterostructures using Molecular-Beam Epitaxy. *Crystal Growth & Design* **2023**, *23* (7), 5001-5007. DOI: 10.1021/acs.cgd.3c00244.
- (19) Li, L. B.; Chen, Z. M.; Zang, Y.; Song, L. X.; Han, Y. L.; Chu, Q. Epitaxial growth of Si/SiC heterostructures with different preferred orientations on 6H-SiC(0001) by LPCVD. *CrystEngComm* **2016**, *18* (30), 5681-5685, 10.1039/C6CE00137H. DOI: 10.1039/C6CE00137H.
- (20) Osbourn, G. C. Strained-layer superlattices from lattice mismatched materials. *Journal of Applied Physics* **1982**, *53* (3), 1586-1589. DOI: 10.1063/1.330615 (accessed 10/24/2023).
- (21) Edward, T. Y.; McCaldin, J. O.; McGill, T. C. Band offsets in semiconductor heterojunctions. In *Solid state physics*, Vol. 46; Elsevier, 1992; pp 1-146.
- (22) Ostheim, L.; Klar, P. J.; Moryson, Y.; Rohnke, M.; Beyer, A.; Volk, M.; Munde, M.; Stolz, W.; Volz, K. Effect of the interface morphology on the lateral electron transport in (001) GaP/Si heterostructures. *Journal of Applied Physics* **2019**, *126* (21), 215704. DOI: 10.1063/1.5124049 (accessed 10/24/2023).
- (23) Baniecki, J. D.; Yamazaki, T.; Ricinschi, D.; Van Overmeere, Q.; Aso, H.; Miyata, Y.; Yamada, H.; Fujimura, N.; Maran, R.; Anazawa, T.; et al. Strain Dependent Electronic Structure and Band Offset Tuning at Heterointerfaces of ASnO₃ (A=Ca, Sr, and Ba) and SrTiO₃. *Scientific Reports* **2017**, *7* (1), 41725. DOI: 10.1038/srep41725.
- (24) Clavel, M. B.; Hudait, M. K. Band Offset Enhancement of a-Al₂O₃/Tensile-Ge for High Mobility Nanoscale pMOS Devices. *IEEE Electron Device Letters* **2017**, *38* (9), 1196-1199. DOI: 10.1109/LED.2017.2734040.
- (25) Lian, S.; Wu, H.; Wu, P.; Sun, H.; An, Y. Strain and interfacial defect tailored electronic structures of two-dimensional WSe₂/h-BN van der Waals heterostructure. *International Journal of Modern Physics B* **2023**, *37* (31), 2350277. DOI: 10.1142/S0217979223502776 (accessed 2023/10/24).
- (26) Park, J.-S.; Jung, Y.-K.; Butler, K. T.; Walsh, A. Quick-start guide for first-principles modelling of semiconductor interfaces. *Journal of Physics: Energy* **2019**, *1* (1), 016001. DOI: 10.1088/2515-7655/aad928.
- (27) Demkowicz, M. J.; Wang, J.; Hoagland, R. G. Chapter 83 - Interfaces Between Dissimilar Crystalline Solids. In *Dislocations in Solids*, Hirth, J. P. Ed.; Vol. 14; Elsevier, 2008; pp 141-205.
- (28) Herbig, M.; Choi, P.; Raabe, D. Combining structural and chemical information at the nanometer scale by correlative transmission electron microscopy and atom probe tomography. *Ultramicroscopy* **2015**, *153*, 32-39. DOI: <https://doi.org/10.1016/j.ultramic.2015.02.003>.
- (29) Merkle, K. L.; Smith, D. J. Atomic Structure of Symmetric Tilt Grain Boundaries in NiO. *Physical Review Letters* **1987**, *59* (25), 2887-2890. DOI: 10.1103/PhysRevLett.59.2887.

- (30) Ruan, Y. C.; Ching, W. Y. An effective dipole model for predicting band offsets in semiconductor heterojunctions. *Journal of Applied Physics* **1986**, *60* (11), 4035-4038. DOI: 10.1063/1.337532 (accessed 10/12/2023).
- (31) Akinci, Ö.; Gürel, H. H.; Ünlü, H. Semi-empirical tight binding modelling of CdSTe/CdTe, ZnSSe/ZnSe and ZnSSe/ CdSe heterostructures. *Thin Solid Films* **2009**, *517* (7), 2431-2437. DOI: <https://doi.org/10.1016/j.tsf.2008.11.040>.
- (32) Zhou, Y.-D.; Zhao, Z.-Y. Interfacial structure and properties of TiO₂ phase junction studied by DFT calculations. *Applied Surface Science* **2019**, *485*, 8-21. DOI: <https://doi.org/10.1016/j.apsusc.2019.04.193>.
- (33) Živković, A.; Mallia, G.; King, H. E.; de Leeuw, N. H.; Harrison, N. M. Mind the Interface Gap: Exposing Hidden Interface Defects at the Epitaxial Heterostructure between CuO and Cu₂O. *ACS Applied Materials & Interfaces* **2022**, *14* (50), 56331-56343. DOI: 10.1021/acsam.2c16889.
- (34) Di Liberto, G.; Tosoni, S.; Pacchioni, G. Z-Scheme versus type-II junction in g-C₃N₄/TiO₂ and g-C₃N₄/SrTiO₃/TiO₂ heterostructures. *Catalysis Science & Technology* **2021**, *11* (10), 3589-3598, 10.1039/D1CY00451D. DOI: 10.1039/D1CY00451D.
- (35) Xue, J.; Bao, J. Interfacial charge transfer of heterojunction photocatalysts: Characterization and calculation. *Surf. Interfaces* **2021**, *25*, 101265. DOI: <https://doi.org/10.1016/j.surfin.2021.101265>.
- (36) Ràfols i Bellés, C.; Selim, S.; Harrison, N. M.; Ahmad, E. A.; Kafizas, A. Beyond band bending in the WO₃/BiVO₄ heterojunction: insight from DFT and experiment. *Sustainable Energy & Fuels* **2019**, *3* (1), 264-271, 10.1039/C8SE00420J. DOI: 10.1039/C8SE00420J.
- (37) Hou, Y.; Li, X. Y.; Zhao, Q. D.; Quan, X.; Chen, G. H. Fabrication of Cu₂O/TiO₂ nanotube heterojunction arrays and investigation of its photoelectrochemical behavior. *Applied Physics Letters* **2009**, *95* (9), 093108. DOI: 10.1063/1.3224181.
- (38) Zhang, J.; Zhu, H.; Zheng, S.; Pan, F.; Wang, T. TiO₂ Film/Cu₂O Microgrid Heterojunction with Photocatalytic Activity under Solar Light Irradiation. *ACS Applied Materials & Interfaces* **2009**, *1* (10), 2111-2114. DOI: 10.1021/am900463g.
- (39) Li, Z.; Liu, J.; Wang, D.; Gao, Y.; Shen, J. Cu₂O/Cu/TiO₂ nanotube Ohmic heterojunction arrays with enhanced photocatalytic hydrogen production activity. *International Journal of Hydrogen Energy* **2012**, *37* (8), 6431-6437. DOI: <https://doi.org/10.1016/j.ijhydene.2012.01.075>.
- (40) Wang, M.; Sun, L.; Lin, Z.; Cai, J.; Xie, K.; Lin, C. p-n Heterojunction photoelectrodes composed of Cu₂O-loaded TiO₂ nanotube arrays with enhanced photoelectrochemical and photoelectrocatalytic activities. *Energy & Environmental Science* **2013**, *6* (4), 1211-1220, 10.1039/C3EE24162A. DOI: 10.1039/C3EE24162A.
- (41) Wang, Y.; Tao, J.; Wang, X.; Wang, Z.; Zhang, M.; He, G.; Sun, Z. A unique Cu₂O/TiO₂ nanocomposite with enhanced photocatalytic performance under visible light irradiation. *Ceramics International* **2017**, *43* (6), 4866-4872. DOI: <https://doi.org/10.1016/j.ceramint.2016.12.130>.
- (42) Abdullah, H.; Kuo, D.-H.; Chen, Y.-H. High-efficient n-type TiO₂/p-type Cu₂O nanodiode photocatalyst to detoxify hexavalent chromium under visible light irradiation. *Journal of Materials Science* **2016**, *51* (17), 8209-8223. DOI: 10.1007/s10853-016-0096-0.
- (43) Liu, Z.; Yan, L. High-efficiency p-n junction oxide photoelectrodes for photoelectrochemical water splitting. *Physical Chemistry Chemical Physics* **2016**, *18* (45), 31230-31237, 10.1039/C6CP06536H. DOI: 10.1039/C6CP06536H.

- (44) Li, Y.; Zhang, W.; Shen, X.; Peng, P.; Xiong, L.; Yu, Y. Octahedral Cu₂O-modified TiO₂ nanotube arrays for efficient photocatalytic reduction of CO₂. *Chinese Journal of Catalysis* **2015**, *36* (12), 2229-2236. DOI: [https://doi.org/10.1016/S1872-2067\(15\)60991-3](https://doi.org/10.1016/S1872-2067(15)60991-3).
- (45) Zhang, J.; Wang, Y.; Yu, C.; Shu, X.; Jiang, L.; Cui, J.; Chen, Z.; Xie, T.; Wu, Y. Enhanced visible-light photoelectrochemical behaviour of heterojunction composite with Cu₂O nanoparticles-decorated TiO₂ nanotube arrays. *New Journal of Chemistry* **2014**, *38* (10), 4975-4984, 10.1039/C4NJ00787E. DOI: 10.1039/C4NJ00787E.
- (46) Xi, Z.; Li, C.; Zhang, L.; Xing, M.; Zhang, J. Synergistic effect of Cu₂O/TiO₂ heterostructure nanoparticle and its high H₂ evolution activity. *International Journal of Hydrogen Energy* **2014**, *39* (12), 6345-6353. DOI: <https://doi.org/10.1016/j.ijhydene.2014.01.209>.
- (47) Sharma, M.; Mandal, M. K.; Pandey, S.; Kumar, R.; Dubey, K. K. Visible-Light-Driven Photocatalytic Degradation of Tetracycline Using Heterostructured Cu₂O–TiO₂ Nanotubes, Kinetics, and Toxicity Evaluation of Degraded Products on Cell Lines. *ACS Omega* **2022**, *7* (37), 33572-33586. DOI: 10.1021/acsomega.2c04576.
- (48) Cerrato, E.; Gionco, C.; Paganini, M. C.; Giamello, E.; Albanese, E.; Pacchioni, G. Origin of Visible Light Photoactivity of the CeO₂/ZnO Heterojunction. *ACS Appl. Energ. Mater.* **2018**, *1* (8), 4247-4260. DOI: 10.1021/acsaem.8b00887.
- (49) Oliveira, M. C.; Fonseca, V. S.; Andrade Neto, N. F.; Ribeiro, R. A. P.; Longo, E.; de Lazaro, S. R.; Motta, F. V.; Bomio, M. R. D. Connecting theory with experiment to understand the photocatalytic activity of CuO–ZnO heterostructure. *Ceramics International* **2020**, *46* (7), 9446-9454. DOI: <https://doi.org/10.1016/j.ceramint.2019.12.205>.
- (50) Li, R.; Zhang, R.; Qiao, Y.; Zhang, D.; Cui, Z.; Wang, W. Heterostructure Ni(OH)₂/ZrO₂ catalyst can achieve efficient oxygen reduction reaction. *Chemical Engineering Science* **2022**, *250*, 117398. DOI: <https://doi.org/10.1016/j.ces.2021.117398>.
- (51) Andrade, A. O. C.; Lacerda, L. H. d. S.; Lage Júnior, M. M.; Sharma, S. K.; Maia da Costa, M. E. H.; Alves, O. C.; Santos, E. C. S.; dos Santos, C. C.; de Menezes, A. S.; San-Miguel, M. A.; et al. Enhanced photocatalytic activity of BiOBr/ZnWO₄ heterojunction: A combined experimental and DFT-based theoretical approach. *Opt. Mater.* **2023**, *138*, 113701. DOI: <https://doi.org/10.1016/j.optmat.2023.113701>.
- (52) Yu, W.; Gui, Q.; Wan, X.; Robertson, J.; Zhang, Z.; Guo, Y. High-throughput interface prediction and generation scheme: The case of β-Ga₂O₃/AlN interfaces. *Applied Physics Letters* **2023**, *123* (16). DOI: 10.1063/5.0162824 (accessed 12/20/2023).
- (53) Hossain, M. T.; Das, M.; Ghosh, J.; Ghosh, S.; Giri, P. K. Understanding the interfacial charge transfer in the CVD grown Bi₂O₂Se/CsPbBr₃ nanocrystal heterostructure and its exploitation in superior photodetection: experiment vs. theory. *Nanoscale* **2021**, *13* (35), 14945-14959, 10.1039/D1NR04470B. DOI: 10.1039/D1NR04470B.
- (54) Zhang, Q.; Zhang, H.; Gu, B.; Tang, Q.; Cao, Q.; Fang, W. Sunlight-driven photocatalytic oxidation of 5-hydroxymethylfurfural over a cuprous oxide-anatase heterostructure in aqueous phase. *Applied Catalysis B: Environmental* **2023**, *320*, 122006. DOI: <https://doi.org/10.1016/j.apcatb.2022.122006>.
- (55) Luttrell, T.; Halpegamage, S.; Tao, J.; Kramer, A.; Sutter, E.; Batzill, M. Why is anatase a better photocatalyst than rutile? - Model studies on epitaxial TiO₂ films. *Scientific Reports* **2014**, *4* (1), 4043. DOI: 10.1038/srep04043.

- (56) Fujishima, A.; Zhang, X.; Tryk, D. A. TiO₂ photocatalysis and related surface phenomena. *Surface Science Reports* **2008**, *63* (12), 515-582. DOI: <https://doi.org/10.1016/j.surfrep.2008.10.001>.
- (57) Schneider, J.; Matsuoka, M.; Takeuchi, M.; Zhang, J.; Horiuchi, Y.; Anpo, M.; Bahnemann, D. W. Understanding TiO₂ Photocatalysis: Mechanisms and Materials. *Chemical Reviews* **2014**, *114* (19), 9919-9986. DOI: 10.1021/cr5001892.
- (58) Ni, M.; Leung, M. K. H.; Leung, D. Y. C.; Sumathy, K. A review and recent developments in photocatalytic water-splitting using TiO₂ for hydrogen production. *Renewable and Sustainable Energy Reviews* **2007**, *11* (3), 401-425. DOI: <https://doi.org/10.1016/j.rser.2005.01.009>.
- (59) Hara, M.; Kondo, T.; Komoda, M.; Ikeda, S.; N. Kondo, J.; Domen, K.; Hara, M.; Shinohara, K.; Tanaka, A. Cu₂O as a photocatalyst for overall water splitting under visible light irradiation. *Chemical Communications* **1998**, (3), 357-358, 10.1039/A707440I. DOI: 10.1039/A707440I.
- (60) Nair, R. V.; Gummaluri, V. S.; Matham, M. V.; C, V. A review on optical bandgap engineering in TiO₂ nanostructures via doping and intrinsic vacancy modulation towards visible light applications. *Journal of Physics D: Applied Physics* **2022**, *55* (31), 313003. DOI: 10.1088/1361-6463/ac6135.
- (61) Pagare, P. K.; Torane, A. Band gap varied cuprous oxide (Cu₂O) thin films as a tool for glucose sensing. *Microchimica Acta* **2016**, *183*, 2983-2989.
- (62) Tamirat, A. G.; Rick, J.; Dubale, A. A.; Su, W.-N.; Hwang, B.-J. Using hematite for photoelectrochemical water splitting: a review of current progress and challenges. *Nanoscale Horizons* **2016**, *1* (4), 243-267, 10.1039/C5NH00098J. DOI: 10.1039/C5NH00098J.
- (63) Durgalakshmi, D.; Ajay Rakkesh, R.; Rajendran, S.; Naushad, M. Principles and Mechanisms of Green Photocatalysis. In *Green Photocatalysts*, Naushad, M., Rajendran, S., Lichtfouse, E. Eds.; Springer International Publishing, 2020; pp 1-24.
- (64) Mohite, S. V.; Kim, S.; Lee, C.; Bae, J.; Kim, Y. Z-scheme heterojunction photocatalyst: Deep eutectic solvents-assisted synthesis of Cu₂O nanocluster improved hydrogen production of TiO₂. *Journal of Alloys and Compounds* **2022**, *928*, 167168. DOI: <https://doi.org/10.1016/j.jallcom.2022.167168>.
- (65) Qiu, P.; Xiong, J.; Lu, M.; Liu, L.; Li, W.; Wen, Z.; Li, W.; Chen, R.; Cheng, G. Integrated p-n/Schottky junctions for efficient photocatalytic hydrogen evolution upon Cu@TiO₂-Cu₂O ternary hybrids with steering charge transfer. *Journal of Colloid and Interface Science* **2022**, *622*, 924-937. DOI: <https://doi.org/10.1016/j.jcis.2022.04.107>.
- (66) Cosma, D.; Urda, A.; Radu, T.; Rosu, M. C.; Mihet, M.; Socaci, C. Evaluation of the Photocatalytic Properties of Copper Oxides/Graphene/TiO₂ Nanoparticles Composites. *Molecules* **2022**, *27* (18), 5803.
- (67) Savchuk, T. P.; Kytina, E. V.; Konstantinova, E. A.; Kytin, V. G.; Pinchuk, O.; Tarhanov, A. K.; Zaitsev, V. B.; Maniecki, T. Photocatalytic CO₂ Conversion Using Anodic TiO₂ Nanotube-Cu₂O Composites. *Catalysts* **2022**, *12* (9), 1011.
- (68) Sun, L.; Han, L.; Li, N.; Wang, P.; Wang, M.; Luo, X.; Li, X. P25-induced polydopamine conformal assembly on Cu₂O polyhedra for hydrophilic and stable photoelectrochemical performance. *Journal of Materials Chemistry C* **2022**, *10* (38), 14194-14201, 10.1039/D2TC03116G. DOI: 10.1039/D2TC03116G.
- (69) Liang, Y.-C.; Li, T.-H. Sputtering-Assisted Synthesis of Copper Oxide–Titanium Oxide Nanorods and Their Photoactive Performances. *Nanomaterials* **2022**, *12* (15), 2634.

- (70) Ahmed, K.; Wang, Y.; Bai, Y.; Sekar, K.; Li, W. A carbon nanowire-promoted Cu₂O/TiO₂ nanocomposite for enhanced photoelectrochemical performance. *New Journal of Chemistry* **2022**, *46* (32), 15495-15503, 10.1039/D2NJ03116G. DOI: 10.1039/D2NJ03116G.
- (71) Goto, H.; Masegi, H.; Sadale, S. B.; Noda, K. Intricate behaviors of gas phase CO₂ photoreduction in high vacuum using Cu₂O-loaded TiO₂ nanotube arrays. *Journal of CO₂ Utilization* **2022**, *59*, 101964. DOI: <https://doi.org/10.1016/j.jcou.2022.101964>.
- (72) Zhang, C.; Huang, Y.; Zhao, B.; Yu, Y.; Yu, Y.; Zhang, B. CuO_x clusters decorated TiO₂ for photocatalytic oxidation of nitrogen in air into nitric oxide under ambient conditions. *Journal of Catalysis* **2022**, *409*, 70-77. DOI: <https://doi.org/10.1016/j.jcat.2022.03.017>.
- (73) Yu, Q.; Fu, Y.; Xiao, K.; Zhang, X.; Du, C.; Chen, J. A label-free photoelectrochemical biosensor with ultra-low-background noise for lead ion assay based on the Cu₂O-CuO-TiO₂ heterojunction. *Analytica Chimica Acta* **2022**, *1195*, 339456. DOI: <https://doi.org/10.1016/j.aca.2022.339456>.
- (74) Cheng, S.-P.; Wei, L.-W.; Wang, H.-P. Photocatalytic Reduction of CO₂ to Methanol by Cu₂O/TiO₂ Heterojunctions. *Sustainability* **2022**, *14* (1), 374.
- (75) Ji, W.; Wang, Y.; Zhang, T. C.; Ouyang, L.; Yuan, S. Heterostructure Cu₂O@TiO₂Nanotube Array Coated Titanium Anode for Efficient Photoelectrocatalytic Oxidation of As(III) in Aqueous Solution. *Industrial & Engineering Chemistry Research* **2021**, *60* (48), 17545-17555. DOI: 10.1021/acs.iecr.1c03420.
- (76) Wang, X.; Jiang, Z.; Chen, H.; Wang, K.; Wang, X. Photocatalytic CO₂ reduction with water vapor to CO and CH₄ in a recirculation reactor by Ag-Cu₂O/TiO₂ Z-scheme heterostructures. *Journal of Alloys and Compounds* **2022**, *896*, 163030. DOI: <https://doi.org/10.1016/j.jallcom.2021.163030>.
- (77) Lv, S.; Wang, Y.; Zhou, Y.; Liu, Q.; Song, C.; Wang, D. Oxygen vacancy stimulated direct Z-scheme of mesoporous Cu₂O/TiO₂ for enhanced photocatalytic hydrogen production from water and seawater. *Journal of Alloys and Compounds* **2021**, *868*, 159144. DOI: <https://doi.org/10.1016/j.jallcom.2021.159144>.
- (78) Zhang, Y.-H.; Liu, M.-M.; Chen, J.-L.; Xie, K.-F.; Fang, S.-M. Dendritic branching Z-scheme Cu₂O/TiO₂ heterostructure photocatalysts for boosting H₂ production. *Journal of Physics and Chemistry of Solids* **2021**, *152*, 109948. DOI: <https://doi.org/10.1016/j.jpcs.2021.109948>.
- (79) Lei, W.; Wang, H.; Zhang, X.; Yang, Z.; Kong, C. Cu₂O-based binary and ternary photocatalysts for the degradation of organic dyes under visible light. *Ceramics International* **2022**, *48* (2), 1757-1764. DOI: <https://doi.org/10.1016/j.ceramint.2021.09.255>.
- (80) Burungale, V.; Seong, C.; Bae, H.; Mane, P.; Ryu, S.-W.; Kang, S.-H.; Ha, J.-S. Surface modification of p/n heterojunction based TiO₂-Cu₂O photoanode with a cobalt-phosphate (CoPi) co-catalyst for effective oxygen evolution reaction. *Applied Surface Science* **2022**, *573*, 151445. DOI: <https://doi.org/10.1016/j.apsusc.2021.151445>.
- (81) Hou, R.; Jia, Y.; Jin, G.; Shi, M.; Jiang, N. Enhanced photocatalytic performance of Cu₂O/TiO₂/rGA composites to degrade gas-phase unsymmetrical dimethylhydrazine. *Journal of Materials Science* **2022**, *57* (5), 3538-3552. DOI: 10.1007/s10853-021-06782-5.
- (82) Wang, S.; Kavaipatti, B.; Kim, S.-J.; Pan, X.; Ramesh, R.; Ager, J. W., III; Wang, L.-W. Atomic and electronic structures of lattice mismatched Cu₂O/TiO₂ interfaces. *Applied Physics Letters* **2014**, *104* (21), 211605. DOI: 10.1063/1.4880942 (accessed 12/20/2023).
- (83) Meng'wa, V.; Makau, N.; Amolo, G.; Scandolo, S.; Seriani, N. Density Functional Theory Study of Water Photo-Oxidation at Copper Oxide Nanostructures on the Anatase (101) Surface.

- The Journal of Physical Chemistry C* **2018**, *122* (29), 16765-16771. DOI: 10.1021/acs.jpcc.8b03671.
- (84) Nie, J.; Yu, X.; Hu, D.; Wang, T.; Liu, Z.; Zhao, N.; Li, J.; Yao, B. Preparation and Properties of Cu₂O/TiO₂ Heterojunction Nanocomposite for Rhodamine B Degradation under Visible Light. *ChemistrySelect* **2020**, *5* (27), 8118-8128. DOI: <https://doi.org/10.1002/slct.202001198> (accessed 2023/12/20).
- (85) Gilbert, T. L. Hohenberg-Kohn theorem for nonlocal external potentials. *Physical Review B* **1975**, *12* (6), 2111.
- (86) Seidl, A.; Görling, A.; Vogl, P.; Majewski, J. A.; Levy, M. Generalized Kohn-Sham schemes and the band-gap problem. *Physical Review B* **1996**, *53* (7), 3764.
- (87) Kresse, G.; Furthmüller, J. Efficient iterative schemes for ab initio total-energy calculations using a plane-wave basis set. *Physical review B* **1996**, *54* (16), 11169.
- (88) Kresse, G.; Hafner, J. Ab initio molecular dynamics for open-shell transition metals. *Physical Review B* **1993**, *48* (17), 13115.
- (89) Kresse, G.; Joubert, D. From ultrasoft pseudopotentials to the projector augmented-wave method. *Physical review b* **1999**, *59* (3), 1758.
- (90) Perdew, J. P.; Burke, K.; Ernzerhof, M. Generalized gradient approximation made simple. *Physical review letters* **1996**, *77* (18), 3865.
- (91) Ernzerhof, M.; Scuseria, G. E. Assessment of the Perdew–Burke–Ernzerhof exchange–correlation functional. *The Journal of chemical physics* **1999**, *110* (11), 5029-5036.
- (92) Krukau, A. V.; Vydrov, O. A.; Izmaylov, A. F.; Scuseria, G. E. Influence of the exchange screening parameter on the performance of screened hybrid functionals. *The Journal of chemical physics* **2006**, *125* (22).
- (93) Heyd, J.; Scuseria, G. E.; Ernzerhof, M. Hybrid functionals based on a screened Coulomb potential. *The Journal of chemical physics* **2003**, *118* (18), 8207-8215.
- (94) Heyd, J.; Scuseria, G. E. Assessment and validation of a screened Coulomb hybrid density functional. *The Journal of chemical physics* **2004**, *120* (16), 7274-7280.
- (95) Blöchl, P. E. Projector augmented-wave method. *Physical review B* **1994**, *50* (24), 17953.
- (96) Monkhorst, H. J.; Pack, J. D. Special points for Brillouin-zone integrations. *Physical review B* **1976**, *13* (12), 5188.
- (97) CRC Handbook of Chemistry and Physics, 86th Edition Edited by David R. Lide (National Institute of Standards and Technology). CRC Press (an imprint of Taylor and Francis Group): Boca Raton, FL. 2005. 2544 pp. \$125.96. ISBN 0-8493-0486-5. *Journal of the American Chemical Society* **2006**, *128* (16), 5585-5585. DOI: 10.1021/ja0598681.
- (98) Werner, A.; Hochheimer, H. D. High-pressure x-ray study of Cu_2O and Ag_2O . *Physical Review B* **1982**, *25* (9), 5929-5934. DOI: 10.1103/PhysRevB.25.5929.
- (99) Burdett, J. K.; Hughbanks, T.; Miller, G. J.; Richardson, J. W., Jr.; Smith, J. V. Structural-electronic relationships in inorganic solids: powder neutron diffraction studies of the rutile and anatase polymorphs of titanium dioxide at 15 and 295 K. *Journal of the American Chemical Society* **1987**, *109* (12), 3639-3646. DOI: 10.1021/ja00246a021.
- (100) Peters, G.; Vill, V. Index of modern inorganic compounds. Subvolume A. Landolt-Börnstein numerical data and functional relationships in science and technology. *Verlag, Berlin* **1989**.
- (101) Burdett, J. K.; Hughbanks, T.; Miller, G. J.; Richardson Jr, J. W.; Smith, J. V. Structural-electronic relationships in inorganic solids: powder neutron diffraction studies of the rutile and

- anatase polymorphs of titanium dioxide at 15 and 295 K. *Journal of the American Chemical Society* **1987**, *109* (12), 3639-3646.
- (102) Vilela Oliveira, D.; Laun, J.; Peintinger, M. F.; Bredow, T. BSSE-correction scheme for consistent gaussian basis sets of double- and triple-zeta valence with polarization quality for solid-state calculations. *Journal of Computational Chemistry* **2019**, *40* (27), 2364-2376. DOI: <https://doi.org/10.1002/jcc.26013>.
- (103) Yin, H.; Wang, X.; Wang, L.; Nie, Q.; Zhang, Y.; Wu, W. Cu₂O/TiO₂ heterostructured hollow sphere with enhanced visible light photocatalytic activity. *Materials Research Bulletin* **2015**, *72*, 176-183. DOI: <https://doi.org/10.1016/j.materresbull.2015.07.030>.
- (104) Zhang, J.; Liu, W.; Wang, X.; Wang, X.; Hu, B.; Liu, H. Enhanced decoloration activity by Cu₂O@TiO₂ nanobelts heterostructures via a strong adsorption-weak photodegradation process. *Applied Surface Science* **2013**, *282*, 84-91. DOI: <https://doi.org/10.1016/j.apsusc.2013.05.054>.
- (105) Bruno, M.; Rubbo, M.; Pastero, L.; Massaro, F. R.; Nestola, F.; Aquilano, D. Computational Approach to the Study of Epitaxy: Natural Occurrence in Diamond/Forsterite and Aragonite/Zabuyelite. *Crystal Growth & Design* **2015**, *15* (6), 2979-2987. DOI: 10.1021/acs.cgd.5b00389.
- (106) Wang, V.; Xu, N.; Liu, J.-C.; Tang, G.; Geng, W.-T. VASPKIT: A user-friendly interface facilitating high-throughput computing and analysis using VASP code. *Computer Physics Communications* **2021**, *267*, 108033. DOI: <https://doi.org/10.1016/j.cpc.2021.108033>.
- (107) Momma, K.; Izumi, F. VESTA 3 for three-dimensional visualization of crystal, volumetric and morphology data. *Journal of Applied Crystallography* **2011**, *44* (6), 1272-1276. DOI: doi:10.1107/S0021889811038970.
- (108) Stukowski, A. Visualization and analysis of atomistic simulation data with OVITO—the Open Visualization Tool. *Modelling and Simulation in Materials Science and Engineering* **2010**, *18* (1), 015012. DOI: 10.1088/0965-0393/18/1/015012.
- (109) Hinuma, Y.; Grüneis, A.; Kresse, G.; Oba, F. Band alignment of semiconductors from density-functional theory and many-body perturbation theory. *Physical Review B* **2014**, *90* (15), 155405. DOI: 10.1103/PhysRevB.90.155405.
- (110) Harnett-Caulfield, L.; Walsh, A. Assessment of interstitial potentials for rapid prediction of absolute band energies in crystals. *The Journal of Chemical Physics* **2021**, *155* (2). DOI: 10.1063/5.0044866 (accessed 1/29/2024).
- (111) Smidstrup, S.; Markussen, T.; Vancraeyveld, P.; Wellendorff, J.; Schneider, J.; Gunst, T.; Verstichel, B.; Stradi, D.; Khomyakov, P. A.; Vej-Hansen, U. G.; et al. QuantumATK: an integrated platform of electronic and atomic-scale modelling tools. *Journal of Physics: Condensed Matter* **2020**, *32* (1), 015901. DOI: 10.1088/1361-648X/ab4007.
- (112) Trenczek-Zajac, A.; Banas-Gac, J.; Radecka, M. TiO₂@Cu₂O n-n Type Heterostructures for Photochemistry. *Materials* **2021**, *14* (13), 3725.
- (113) Liao, Y.; Deng, P.; Wang, X.; Zhang, D.; Li, F.; Yang, Q.; Zhang, H.; Zhong, Z. A Facile Method for Preparation of Cu₂O-TiO₂ NTA Heterojunction with Visible-Photocatalytic Activity. *Nanoscale Res Lett* **2018**, *13* (1), 221. DOI: 10.1186/s11671-018-2637-8.
- (114) Qi, L.; Wang, M.; Xue, J.; Zhang, Q.; Chen, F.; Liu, Q.; Li, W.; Li, X. Simultaneous Tuning Band Gaps of Cu₂O and TiO₂ to Form S-Scheme Hetero-Photocatalyst. *Chemistry – A European Journal* **2021**, *27* (59), 14638-14644. DOI: <https://doi.org/10.1002/chem.202102120> (accessed 2023/12/20).

- (115) Cahen, D.; Kahn, A. Electron Energetics at Surfaces and Interfaces: Concepts and Experiments. *Advanced Materials* **2003**, *15* (4), 271-277. DOI: <https://doi.org/10.1002/adma.200390065> (accessed 2023/10/12).
- (116) Ping, Y.; Rocca, D.; Galli, G. Electronic excitations in light absorbers for photoelectrochemical energy conversion: first principles calculations based on many body perturbation theory. *Chemical Society Reviews* **2013**, *42* (6), 2437-2469, 10.1039/C3CS00007A. DOI: 10.1039/C3CS00007A.
- (117) Hinuma, Y.; Kumagai, Y.; Tanaka, I.; Oba, F. Band alignment of semiconductors and insulators using dielectric-dependent hybrid functionals: Toward high-throughput evaluation. *Physical Review B* **2017**, *95* (7), 075302. DOI: 10.1103/PhysRevB.95.075302.
- (118) Li, L.; Mi, J.; Yong, Y.; Mao, B.; Shi, W. First-principles study on the lattice plane and termination dependence of the electronic properties of the NiO/CH₃NH₃PbI₃ interfaces. *Journal of Materials Chemistry C* **2018**, *6* (30), 8226-8233, 10.1039/C8TC01974F. DOI: 10.1039/C8TC01974F.
- (119) Tasker, P. W. The stability of ionic crystal surfaces. *Journal of Physics C: Solid State Physics* **1979**, *12* (22), 4977. DOI: 10.1088/0022-3719/12/22/036.
- (120) Noguera, C. *Physics and Chemistry at Oxide Surfaces*; Cambridge University Press, 1996. DOI: DOI: 10.1017/CBO9780511524301.
- (121) Noguera, C. Polar oxide surfaces. *Journal of Physics: Condensed Matter* **2000**, *12* (31), R367.
- (122) Ferrer, M. M.; Fabris, G. S. L.; de Faria, B. V.; Martins, J. B. L.; Moreira, M. L.; Sambrano, J. R. Quantitative evaluation of the surface stability and morphological changes of Cu₂O particles. *Heliyon* **2019**, *5* (10), e02500. DOI: <https://doi.org/10.1016/j.heliyon.2019.e02500>.
- (123) Soon, A.; Söhnel, T.; Idriss, H. Plane-wave pseudopotential density functional theory periodic slab calculations of CO adsorption on Cu₂O(111) surface. *Surface Science* **2005**, *579* (2), 131-140. DOI: <https://doi.org/10.1016/j.susc.2005.01.038>.
- (124) Hejna, J.; Radojewska, E. B.; Szymański, H.; Wolcyrz, M. Determination of the lattice mismatch in heterostructures by X-ray diffraction in the SEM. *Scanning* **1986**, *8* (4), 177-181. DOI: <https://doi.org/10.1002/sca.4950080405>.
- (125) Ohtake, A.; Mano, T.; Sakuma, Y. Strain relaxation in InAs heteroepitaxy on lattice-mismatched substrates. *Scientific Reports* **2020**, *10* (1), 4606. DOI: 10.1038/s41598-020-61527-9.
- (126) Manasreh, O. *Semiconductor heterojunctions and nanostructures*; 2005.
- (127) Physics and Properties of Semiconductors—A Review. In *Physics of Semiconductor Devices*, 2006; pp 5-75.
- (128) Di Liberto, G.; Pacchioni, G. Band offset in semiconductor heterojunctions. *Journal of Physics: Condensed Matter* **2021**, *33* (41), 415002. DOI: 10.1088/1361-648X/ac1620.
- (129) Steiner, K.; Chen, W.; Pasquarello, A. Band offsets of lattice-matched semiconductor heterojunctions through hybrid functionals and $\{G\}_{0}\{W\}_{0}$. *Physical Review B* **2014**, *89* (20), 205309. DOI: 10.1103/PhysRevB.89.205309.
- (130) Kleinman, L. Comment on the average potential of a Wigner solid. *Physical Review B* **1981**, *24* (12), 7412-7414. DOI: 10.1103/PhysRevB.24.7412.
- (131) Baroni, S.; Resta, R.; Baldereschi, A.; Peressi, M. Can We Tune the Band Offset at Semiconductor Heterojunctions? In *Spectroscopy of Semiconductor Microstructures*, Fasol, G., Fasolino, A., Lugli, P. Eds.; Springer US, 1989; pp 251-271.

- (132) Van de Walle, C. G.; Martin, R. M. Theoretical study of band offsets at semiconductor interfaces. *Physical Review B* **1987**, *35* (15), 8154-8165. DOI: 10.1103/PhysRevB.35.8154.
- (133) Baldereschi, A.; Baroni, S.; Resta, R. Band Offsets in Lattice-Matched Heterojunctions: A Model and First-Principles Calculations for GaAs/AlAs. *Physical Review Letters* **1988**, *61* (6), 734-737. DOI: 10.1103/PhysRevLett.61.734.
- (134) Conesa, J. C. Modeling with Hybrid Density Functional Theory the Electronic Band Alignment at the Zinc Oxide–Anatase Interface. *The Journal of Physical Chemistry C* **2012**, *116* (35), 18884-18890. DOI: 10.1021/jp306160c.
- (135) Shaltaf, R.; Rignanese, G. M.; Gonze, X.; Giustino, F.; Pasquarello, A. Band Offsets at the Si/SiO_2 Interface from Many-Body Perturbation Theory. *Physical Review Letters* **2008**, *100* (18), 186401. DOI: 10.1103/PhysRevLett.100.186401.
- (136) Mori-Sánchez, P.; Cohen, A. J.; Yang, W. Localization and Delocalization Errors in Density Functional Theory and Implications for Band-Gap Prediction. *Physical Review Letters* **2008**, *100* (14), 146401. DOI: 10.1103/PhysRevLett.100.146401.
- (137) Ramprasad, R.; Zhu, H.; Rinke, P.; Scheffler, M. New Perspective on Formation Energies and Energy Levels of Point Defects in Nonmetals. *Physical Review Letters* **2012**, *108* (6), 066404. DOI: 10.1103/PhysRevLett.108.066404.
- (138) Weston, L.; Taylor, H.; Krishnaswamy, K.; Bjaalie, L.; Van de Walle, C. G. Accurate and efficient band-offset calculations from density functional theory. *Computational Materials Science* **2018**, *151*, 174-180. DOI: <https://doi.org/10.1016/j.commatsci.2018.05.002>.
- (139) Peressi, M.; Baldereschi, A.; Baroni, S. 2 - Ab initio studies of structural and electronic properties. In *Characterization of Semiconductor Heterostructures and Nanostructures*, Lamberti, C. Ed.; Elsevier, 2008; pp 17-54.
- (140) Franciosi, A.; Van de Walle, C. G. Heterojunction band offset engineering. *Surface Science Reports* **1996**, *25* (1), 1-140. DOI: [https://doi.org/10.1016/0167-5729\(95\)00008-9](https://doi.org/10.1016/0167-5729(95)00008-9).
- (141) Alkauskas, A.; Broqvist, P.; Devynck, F.; Pasquarello, A. Band Offsets at Semiconductor-Oxide Interfaces from Hybrid Density-Functional Calculations. *Physical Review Letters* **2008**, *101* (10), 106802. DOI: 10.1103/PhysRevLett.101.106802.
- (142) Hybertsen, M. S.; Louie, S. G. Electron correlation in semiconductors and insulators: Band gaps and quasiparticle energies. *Physical Review B* **1986**, *34* (8), 5390-5413. DOI: 10.1103/PhysRevB.34.5390.
- (143) Zhu, X.; Louie, S. G. Quasiparticle band structure of thirteen semiconductors and insulators. *Physical Review B* **1991**, *43* (17), 14142-14156. DOI: 10.1103/PhysRevB.43.14142.
- (144) Chen, W.; Pasquarello, A. Band-edge positions in GW : Effects of starting point and self-consistency. *Physical Review B* **2014**, *90* (16), 165133. DOI: 10.1103/PhysRevB.90.165133.
- (145) Aguirre, M. E.; Zhou, R.; Eugene, A. J.; Guzman, M. I.; Grela, M. A. Cu₂O/TiO₂ heterostructures for CO₂ reduction through a direct Z-scheme: Protecting Cu₂O from photocorrosion. *Applied Catalysis B: Environmental* **2017**, *217*, 485-493. DOI: <https://doi.org/10.1016/j.apcatb.2017.05.058>.
- (146) Liu, L.; Yang, W.; Sun, W.; Li, Q.; Shang, J. K. Creation of Cu₂O@TiO₂ Composite Photocatalysts with p–n Heterojunctions Formed on Exposed Cu₂O Facets, Their Energy Band Alignment Study, and Their Enhanced Photocatalytic Activity under Illumination with Visible Light. *ACS Applied Materials & Interfaces* **2015**, *7* (3), 1465-1476. DOI: 10.1021/am505861c.
- (147) Asadinamin, M.; Živkovic, A.; Ullrich, S.; Meyer, H.; Zhao, Y. Charge Dynamics of a CuO Thin Film on Picosecond to Microsecond Timescales Revealed by Transient Absorption

- Spectroscopy. *ACS Applied Materials & Interfaces* **2023**, *15* (14), 18414-18426. DOI: 10.1021/acsami.2c22595.
- (148) Janczarek, M.; Endo, M.; Zhang, D.; Wang, K.; Kowalska, E. Enhanced Photocatalytic and Antimicrobial Performance of Cuprous Oxide/Titania: The Effect of Titania Matrix. *Materials* **2018**, *11* (11), 2069.
- (149) Ibrahim, M. M.; Mezni, A.; El-Sheshtawy, H. S.; Abu Zaid, A. A.; Alsawat, M.; El-Shafi, N.; Ahmed, S. I.; Shaltout, A. A.; Amin, M. A.; Kumeria, T.; Altalhi, T. Direct Z-scheme of Cu₂O/TiO₂ enhanced self-cleaning, antibacterial activity, and UV protection of cotton fiber under sunlight. *Applied Surface Science* **2019**, *479*, 953-962. DOI: <https://doi.org/10.1016/j.apsusc.2019.02.169>.
- (150) Messaadia, L.; Kiamouche, S.; Lahmar, H.; Masmoudi, R.; Boulahbel, H.; Trari, M.; Benamira, M. Solar photodegradation of Rhodamine B dye by Cu₂O/TiO₂ heterostructure: experimental and computational studies of degradation and toxicity. *Journal of Molecular Modeling* **2023**, *29* (2), 38. DOI: 10.1007/s00894-023-05449-z.
- (151) Zhang, X.; Han, D.; Dai, M.; Chen, K.; Han, Z.; Fan, Y.; He, Y.; Han, D.; Niu, L. Enhanced photocatalytic degradation of tetracycline by constructing a controllable Cu₂O–TiO₂ heterojunction with specific crystal facets. *Catalysis Science & Technology* **2021**, *11* (18), 6248-6256, 10.1039/D1CY00761K. DOI: 10.1039/D1CY00761K.

Supplementary information

Interfacial Morphology and Band Bending in anatase $\text{TiO}_2/\text{Cu}_2\text{O}$ Heterostructures

Mona Asadinamin,¹ Aleksandar Živkovic^{2,3}, Nora H. De Leeuw², and Steven P. Lewis¹

¹ Department of Physics and Astronomy, University of Georgia, Athens, Georgia 30602, US

² Department of Earth Sciences, Utrecht University, Princetonlaan 8a, 3548CB Utrecht, The Netherlands

³ Institut für Theoretische Physik und Astrophysik, Christian-Albrechts-Universität zu Kiel, Leibnizstraße 15, 24118 Kiel, Germany

Corresponding author: a.zivkovic@uu.nl, splewis@uga.edu

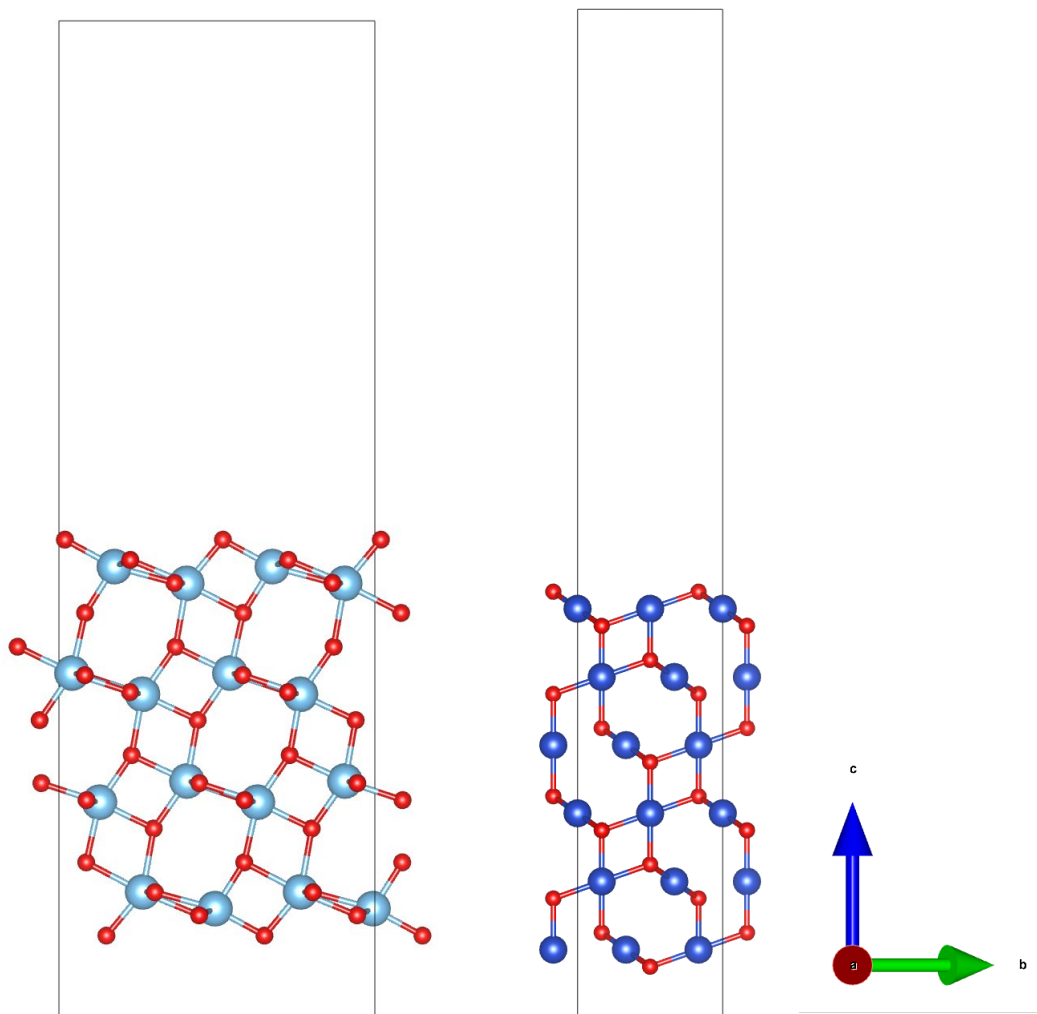


Figure 10. Side view of the slab morphologies of the 4-bilayer TiO_2 (101) surface (left) and 6-trilayer Cu_2O (111) surface (right). Ti: light blue, oxygen: red, and cu: dark blue. The coordinate system is shown by the blue and green arrows where c indicates the non-periodic direction.

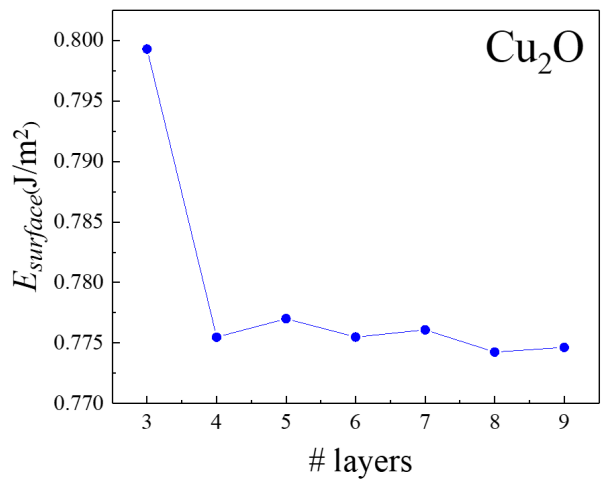
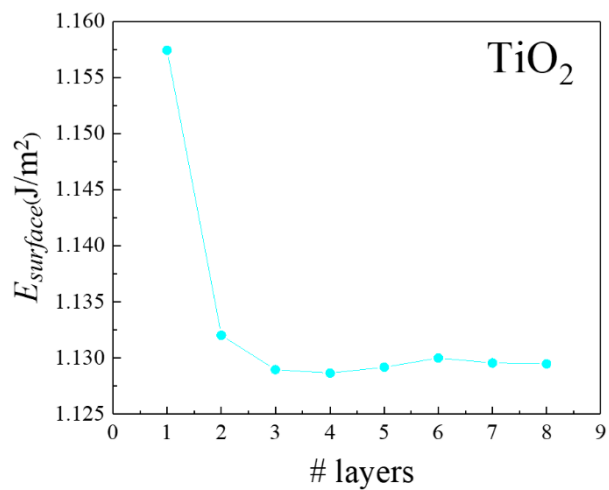


Figure 11. Surface energies of the relaxed TiO₂ (left) and Cu₂O (right) slabs which quickly converged to a value of approximately 1.22 J/m² for a 4-bilayer TiO₂ and 0.77 J/m² for a 4-trilayer Cu₂O.

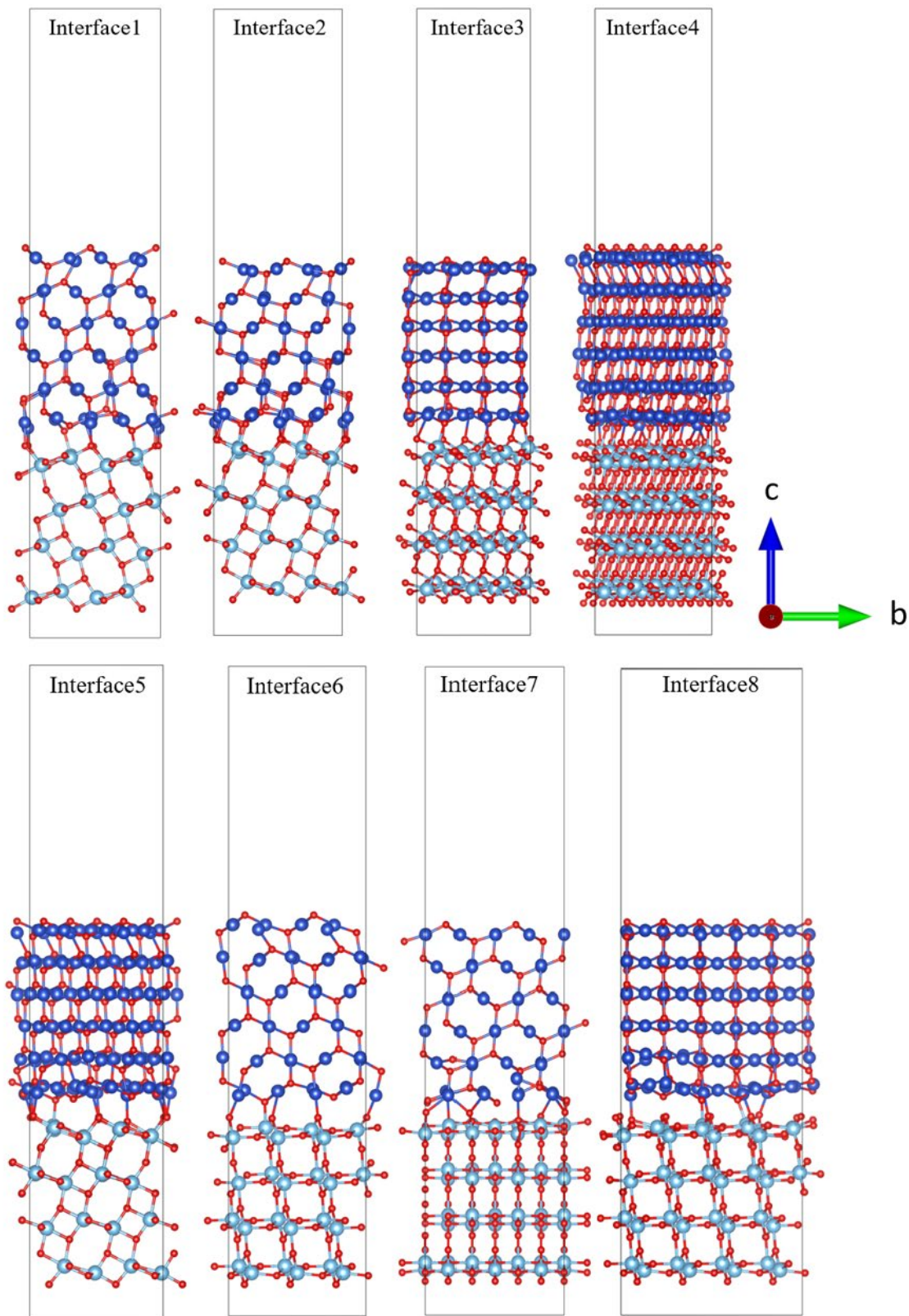


Figure 12. Side view unit cell of the relaxed structure of interfaces 1-8. The green and blue arrows show the coordinate systems.

Table S2. Computed values of electronic band gap, ionization potential (IP), and electron affinity (EA) for Cu₂O and TiO₂.

Compound	XC	Kohn-Sham gap (eV)	IP (eV)	EA (eV)	Exp. (eV)
Cu ₂ O	PBE	0.46	4.64	4.18	5.0 eV to 4.0 eV (IP ¹)
	HSE06	1.94	5.81	3.87	3.20 eV (EA ²)
TiO ₂	PBE	1.94	7.00	5.03	7.96 (IP ³)
	HSE06	3.34	8.84	5.30	5.1 to 5.3 eV (EA ⁴)

Table S3. Computed valence band and conduction band offsets at the Cu₂O / TiO₂ interface using two different approaches, the independent compounds alignment and the alignment based on an explicitly modelled interfacial structure.

System	XC	Valence band offset (independent compound alignment) (eV)	Conduction band offset (independent compound alignment) (eV)	Valence band offset (explicit interface) (eV)	Conduction band offset (explicit interface) (eV)
Cu ₂ O(111) / TiO ₂ (101)	PBE	2.35	0.84	1.93	0.42
	HSE06	2.83	1.43	1.92 ¹	0.52

¹ The potential offset at the interface was taken from PBE calculations, assuming transferability of values as outlined in the work of (5) Conesa, J. C. Modeling with Hybrid Density Functional Theory the Electronic Band Alignment at the Zinc Oxide–Anatase Interface. *The Journal of Physical Chemistry C* **2012**, *116* (35), 18884-18890. DOI: 10.1021/jp306160c..

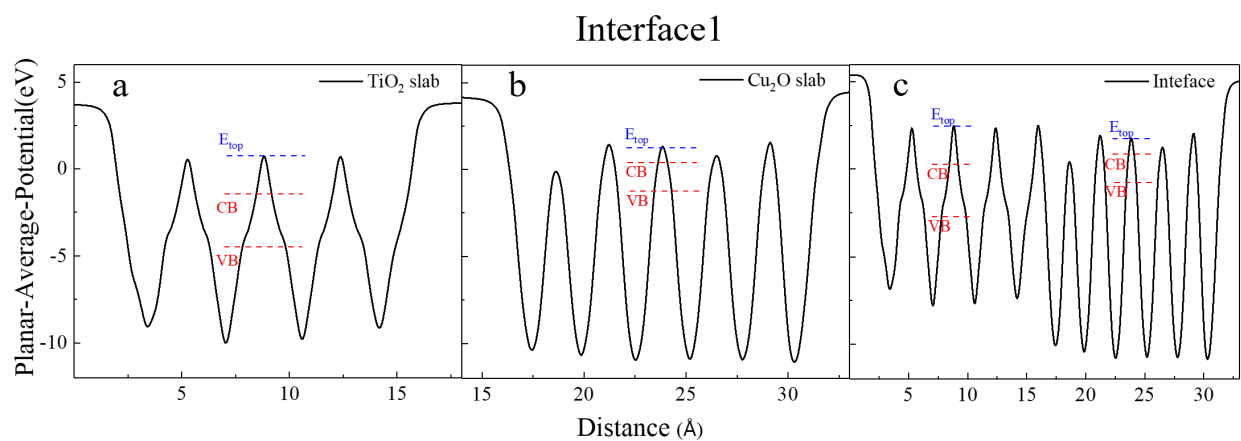


Figure 13. planar-averaged electrostatic potentials in the x - y plane of (a,b) the isolated slabs with the interface geometries, and (c) of interface 1 as a function of the distance along the z -direction, normal to the interface.

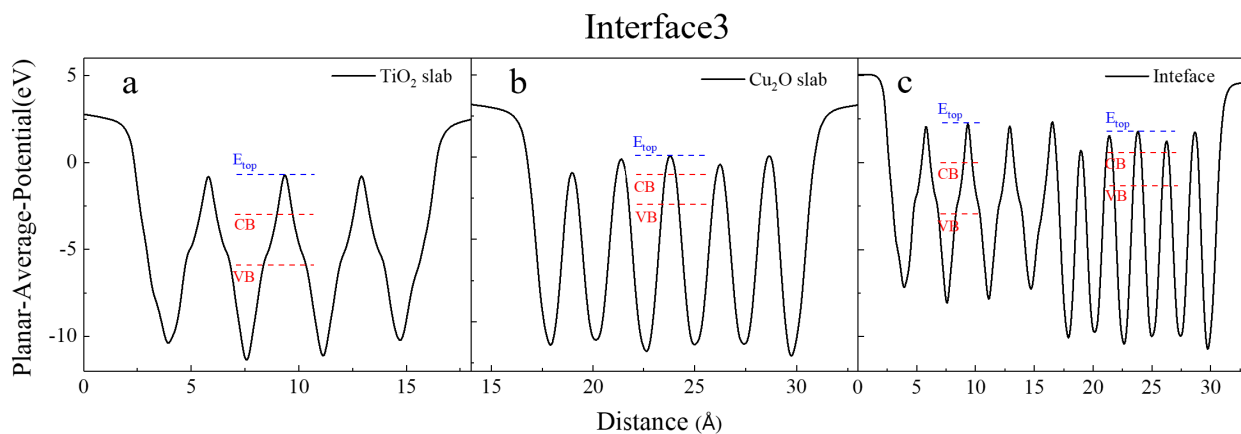


Figure 14. planar-averaged electrostatic potentials in the x - y plane of (a,b) the isolated slabs with the interface geometries, and (c) of interface 3 as a function of the distance along the z -direction, normal to the interface.

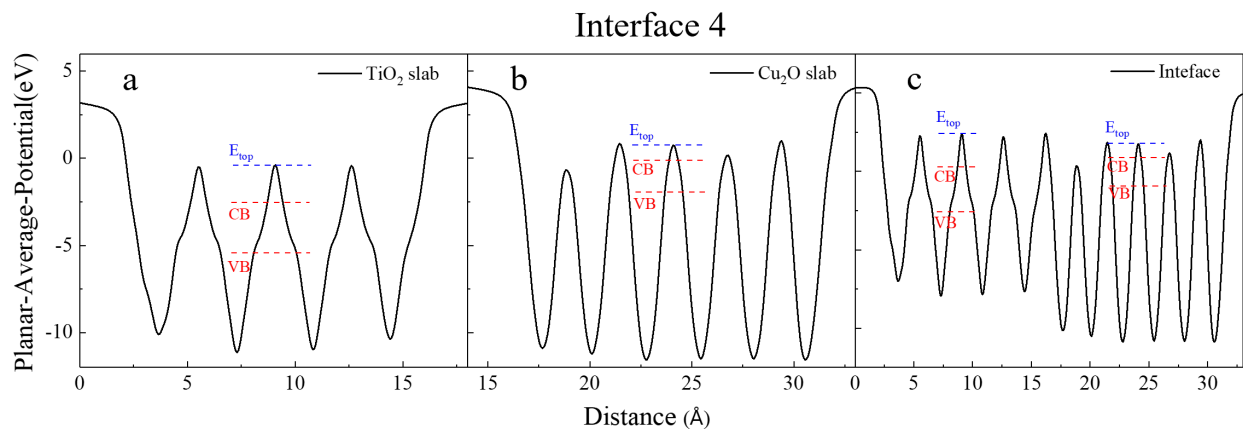


Figure 15. planar-averaged electrostatic potentials in the x - y plane of (a,b) the isolated slabs with the interface geometries, and (c) of interface 4 as a function of the distance along the z -direction, normal to the interface.

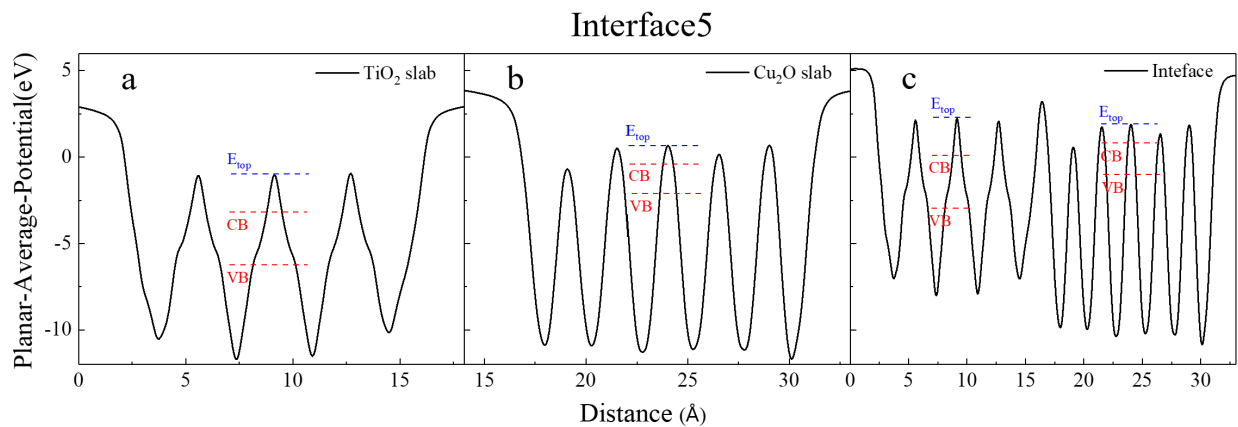


Figure 16. planar-averaged electrostatic potentials in the x - y plane of (a,b) the isolated slabs with the interface geometries, and (c) of interface 5 as a function of the distance along the z -direction, normal to the interface.

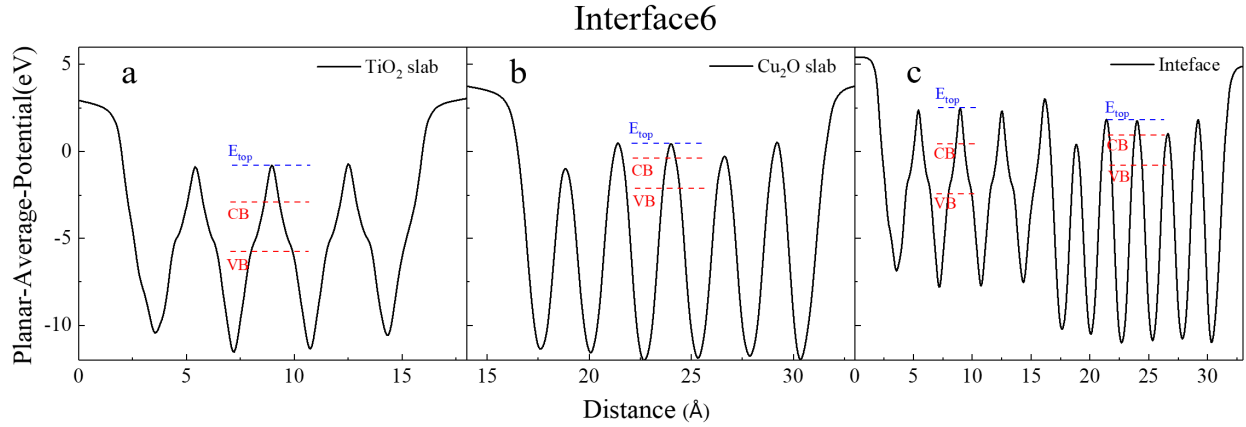


Figure 17. planar-averaged electrostatic potentials in the x - y plane of (a,b) the isolated slabs with the interface geometries, and (c) of interface 6 as a function of the distance along the z -direction, normal to the interface.

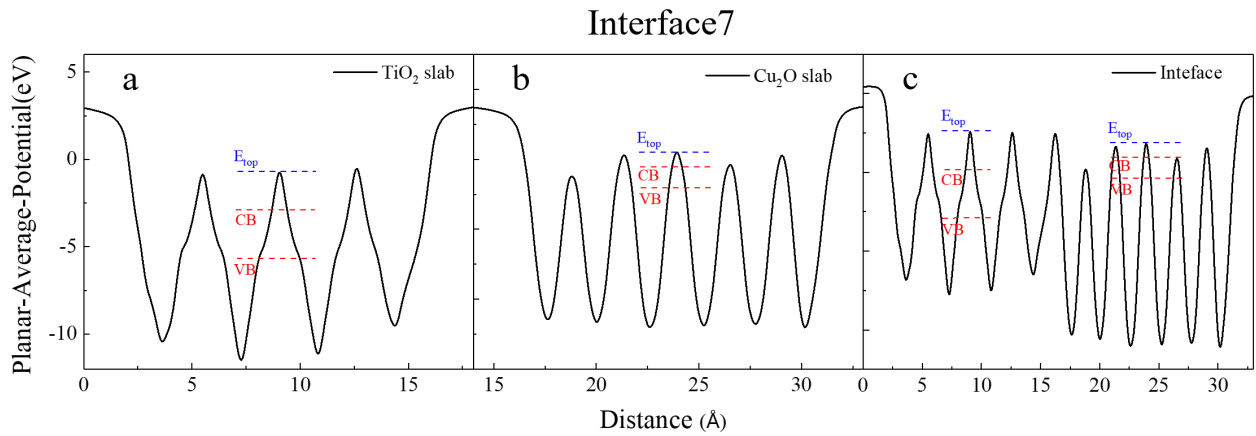


Figure 18. planar-averaged electrostatic potentials in the x - y plane of (a,b) the isolated slabs with the interface geometries, and (c) of interface 7 as a function of the distance along the z -direction, normal to the interface.

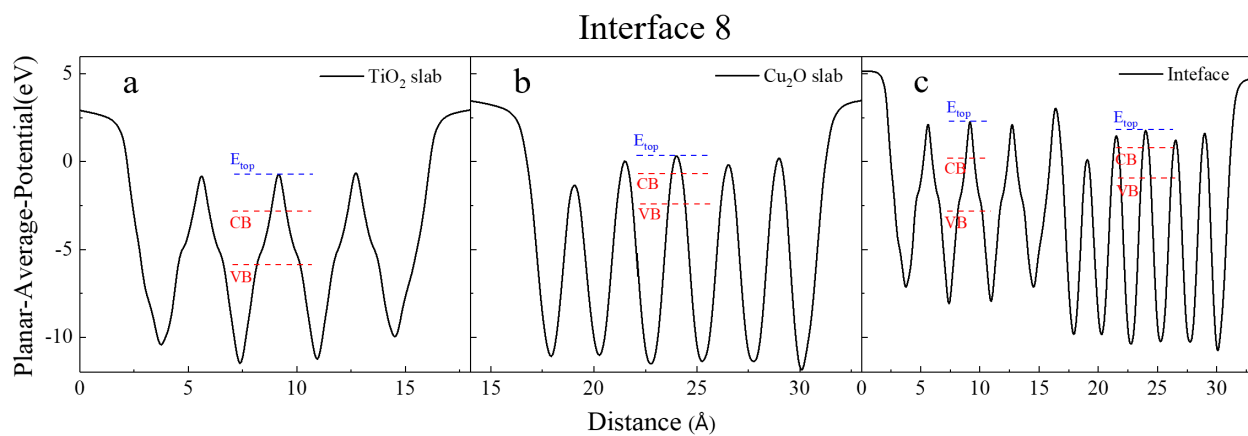


Figure 19. planar-averaged electrostatic potentials in the x - y plane of (a,b) the isolated slabs with the interface geometries, and (c) of interface 8 as a function of the distance along the z -direction, normal to the interface.

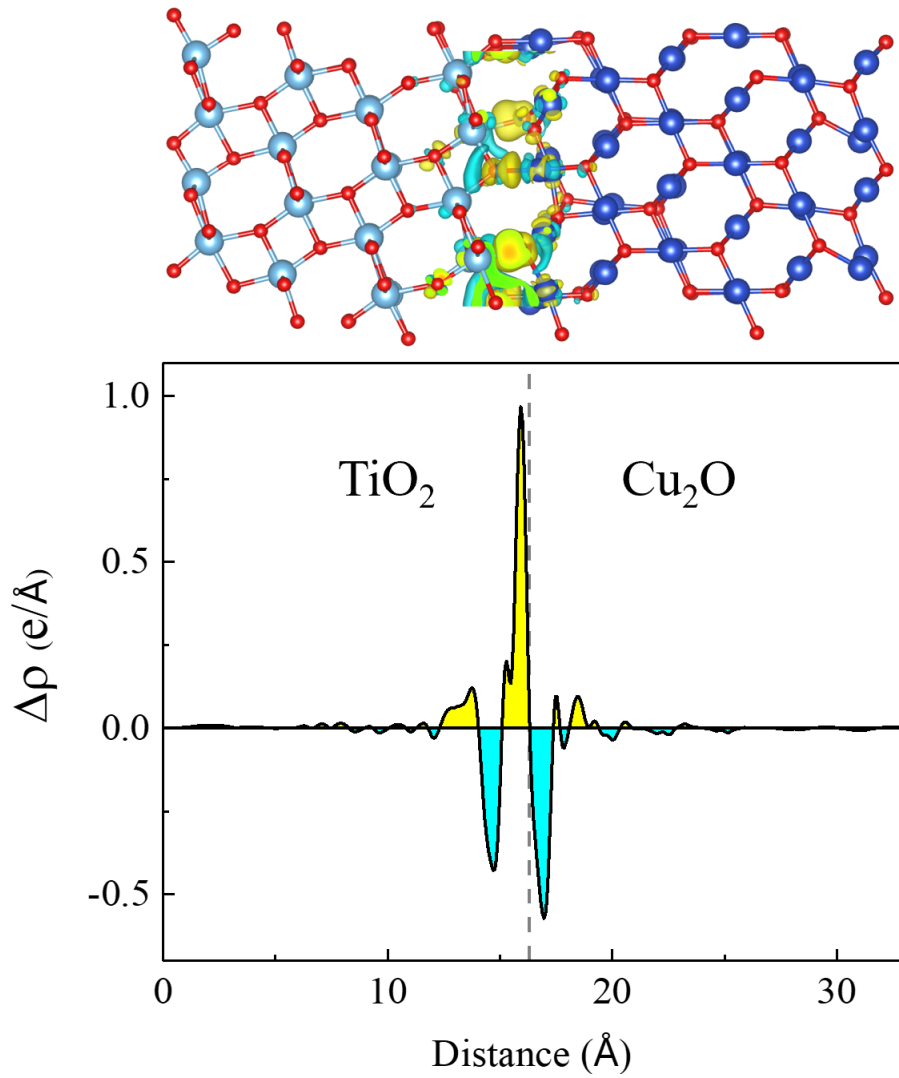


Figure 20. Charge density difference of interface 1. Yellow: charge accumulation. Cyan: charge depletion. The dashed line represents the midpoint layer of the interface.

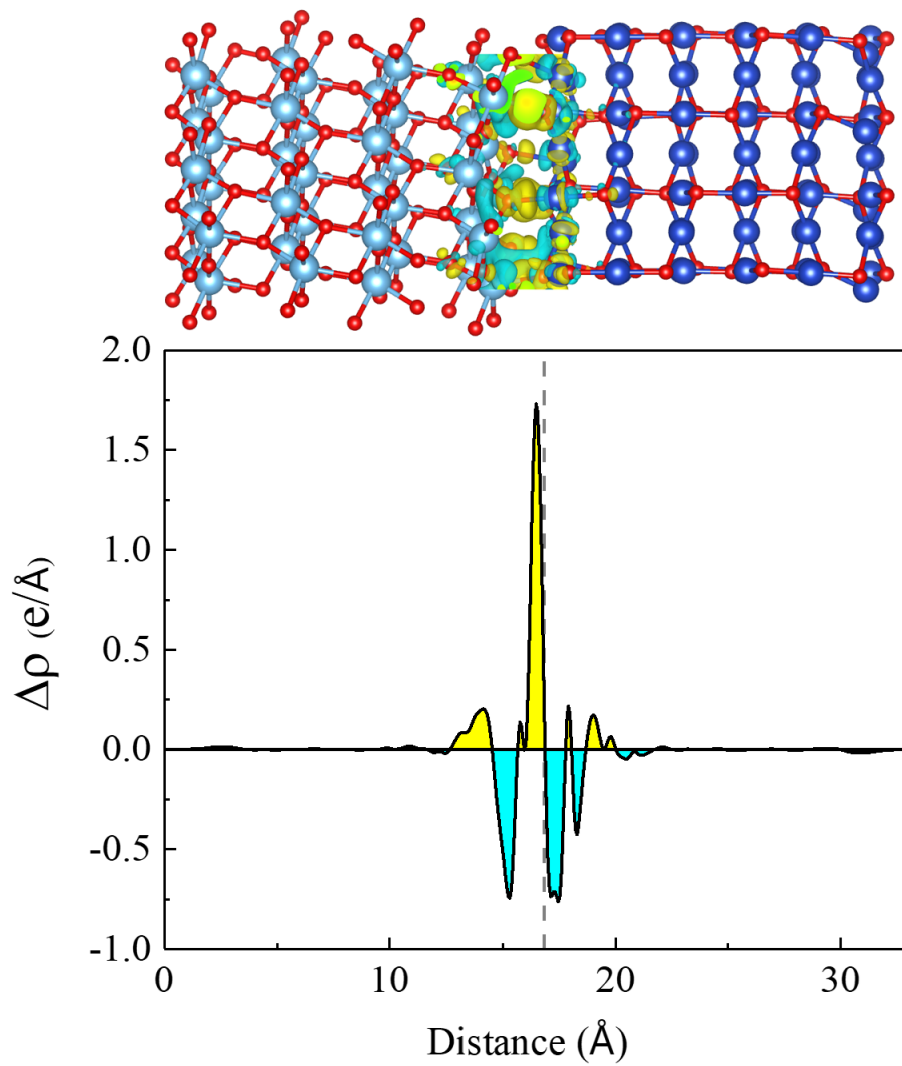


Figure 21. Charge density difference of interface 3. Yellow: charge accumulation. Cyan: charge depletion. The dashed line represents the midpoint layer of the interface.

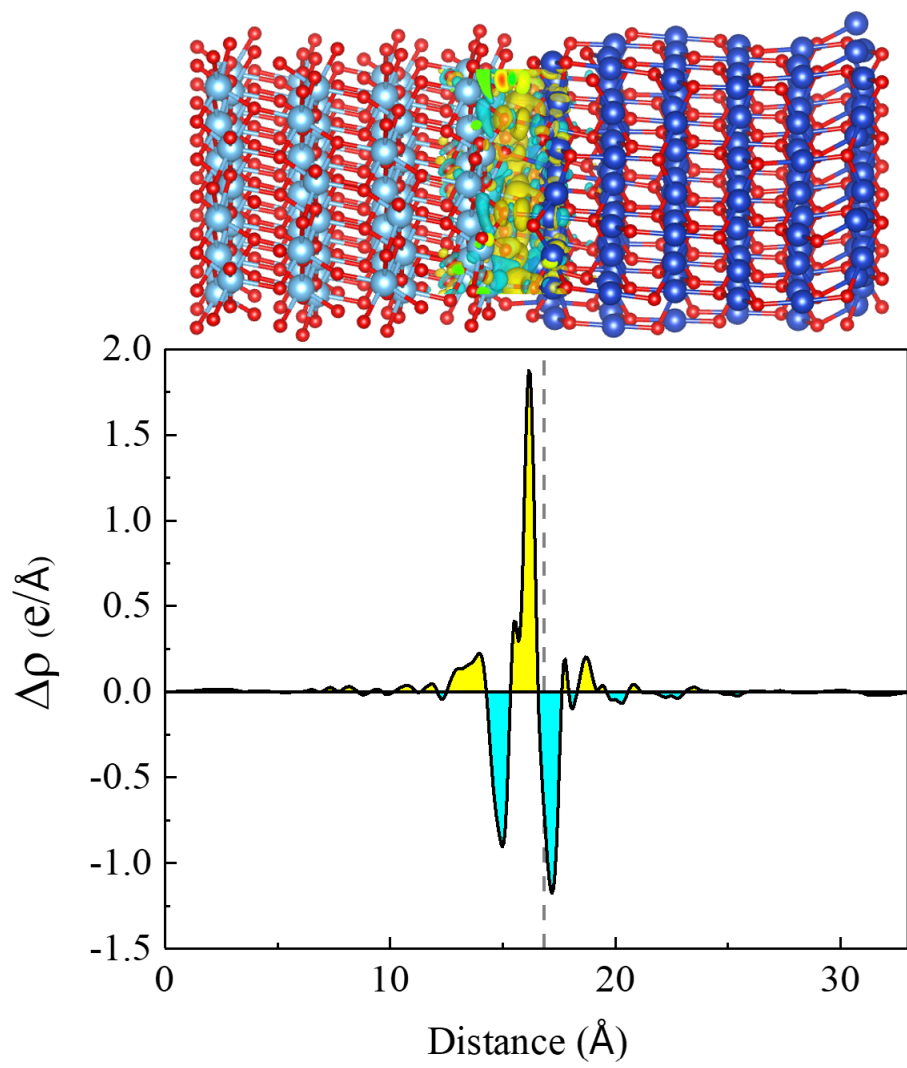


Figure 22. Charge density difference of interface 4. Yellow: charge accumulation. Cyan: charge depletion. The dashed line represents the midpoint layer of the interface.

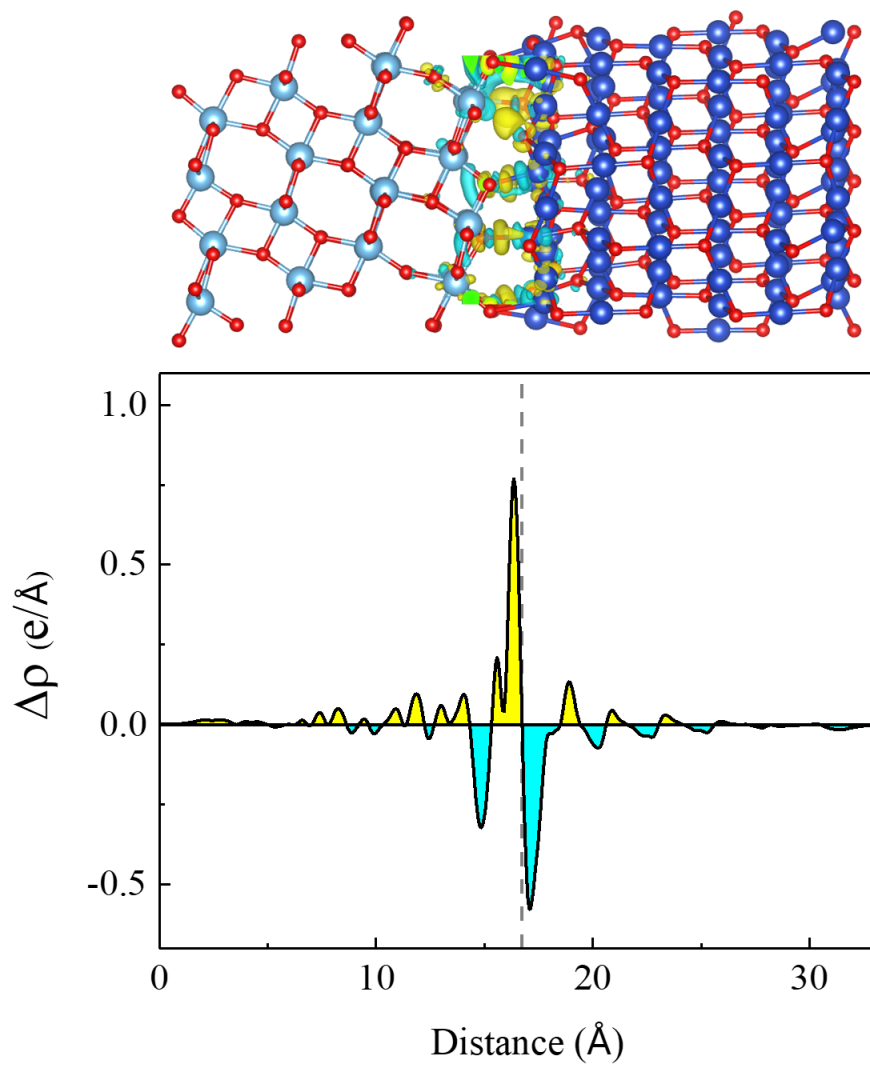


Figure 23. Charge density difference of interface 5. Yellow: charge accumulation. Cyan: charge depletion. The dashed line represents the midpoint layer of the interface.

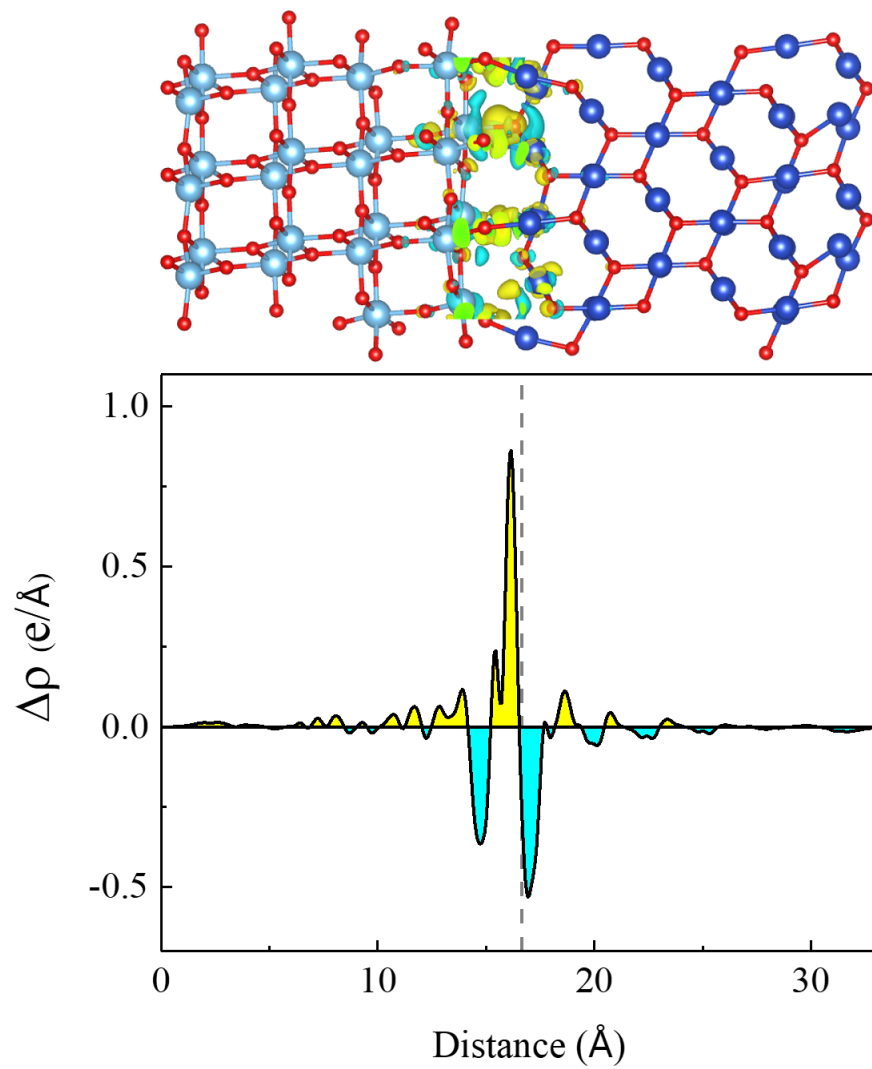


Figure 24. Charge density difference of interface 6. Yellow: charge accumulation. Cyan: charge depletion. The dashed line represents the midpoint layer of the interface.

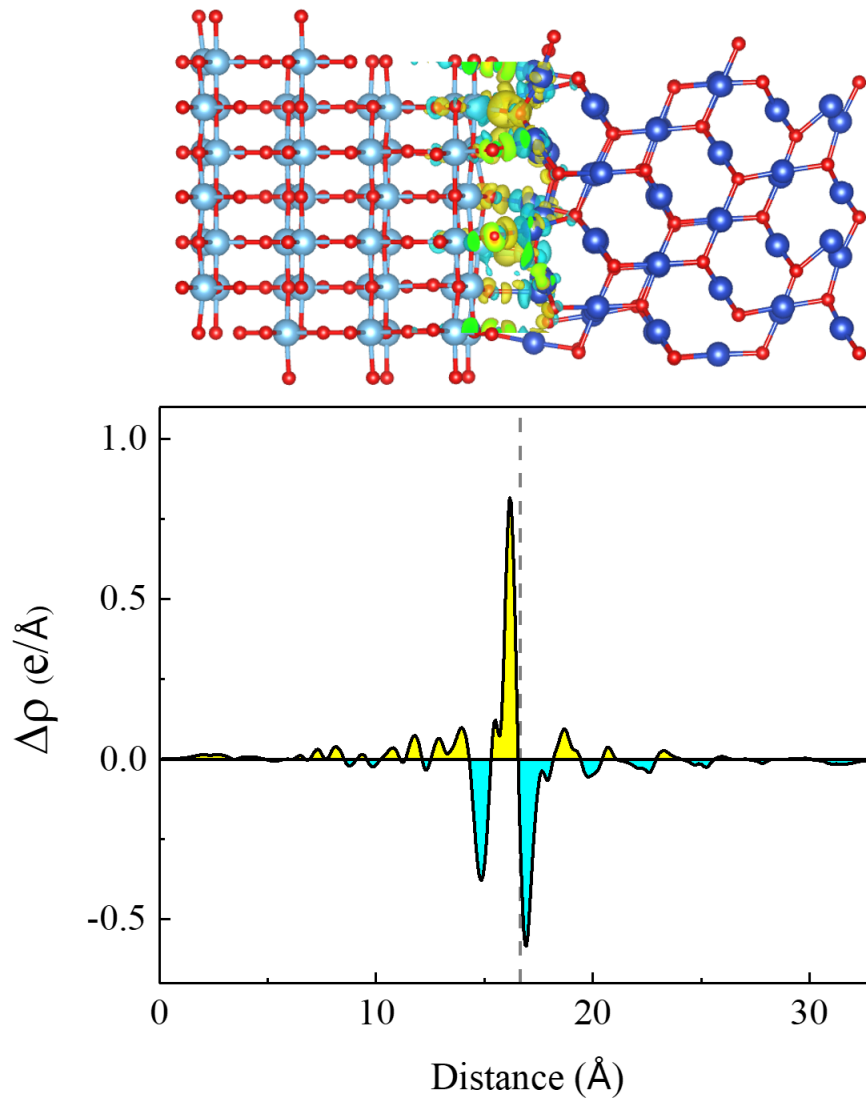


Figure 25. Charge density difference of interface 7. Yellow: charge accumulation. Cyan: charge depletion. The dashed line represents the midpoint layer of the interface.

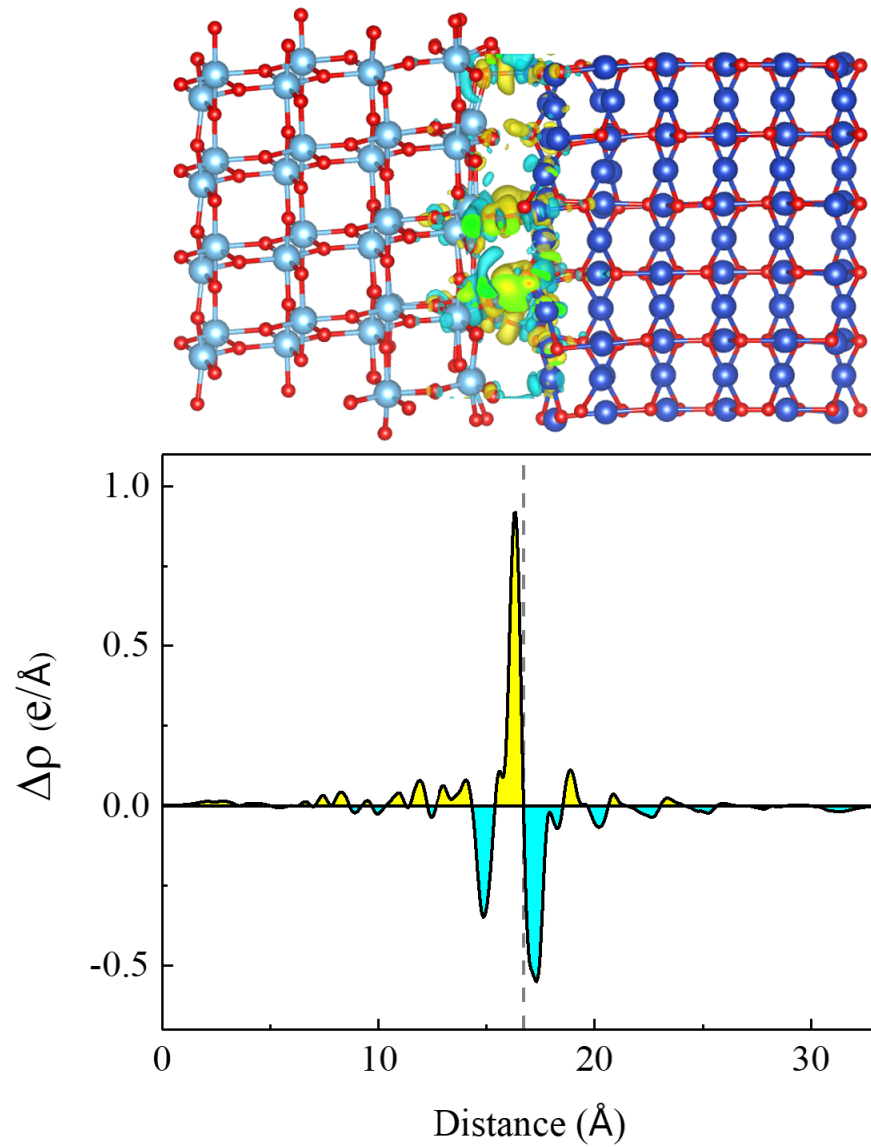


Figure 26. Charge density difference of interface 8. Yellow: charge accumulation. Cyan: charge depletion. The dashed line represents the midpoint layer of the interface.

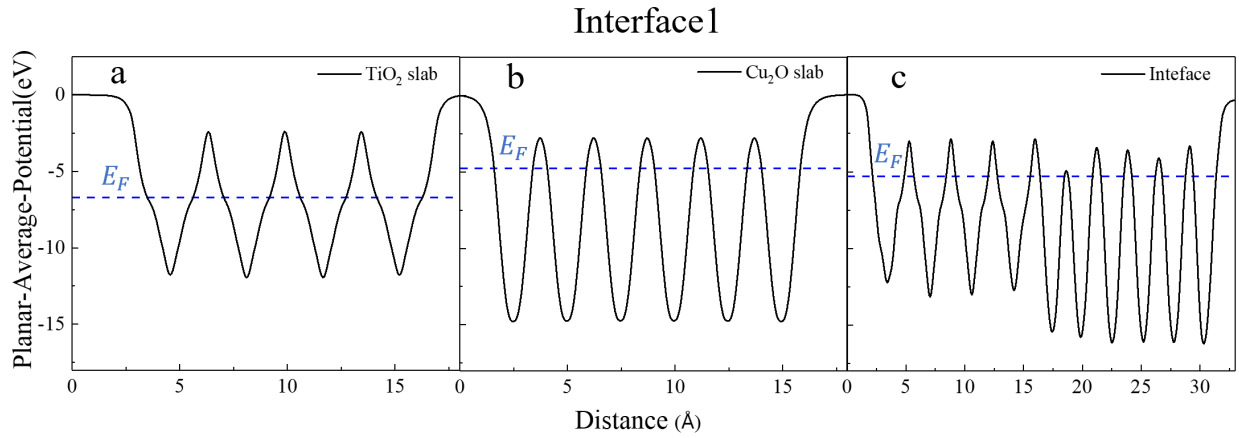


Figure 27. Fermi energy assessment of interface 1 (a,b) before and (c) after contact

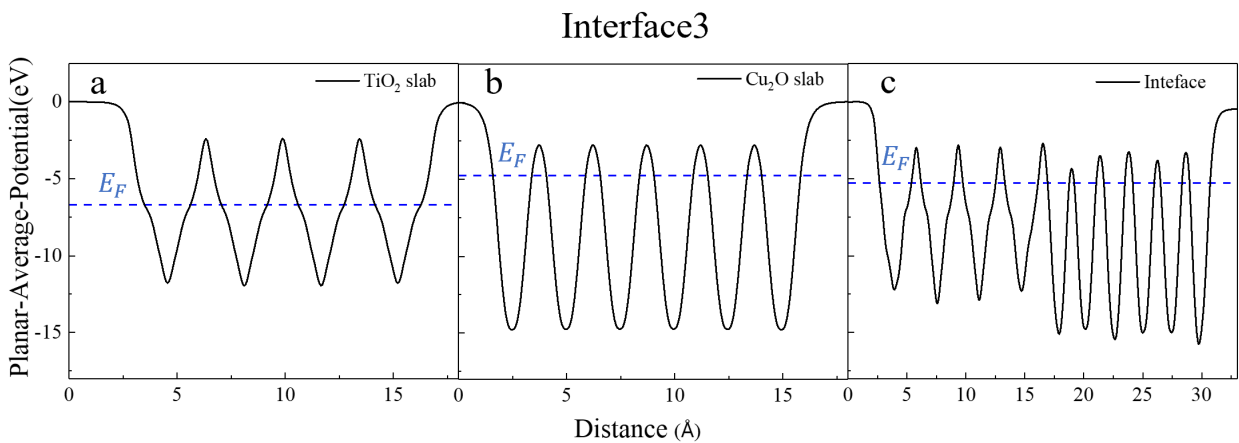


Figure 28. Fermi energy assessment of interface 3 (a,b) before and (c) after contact

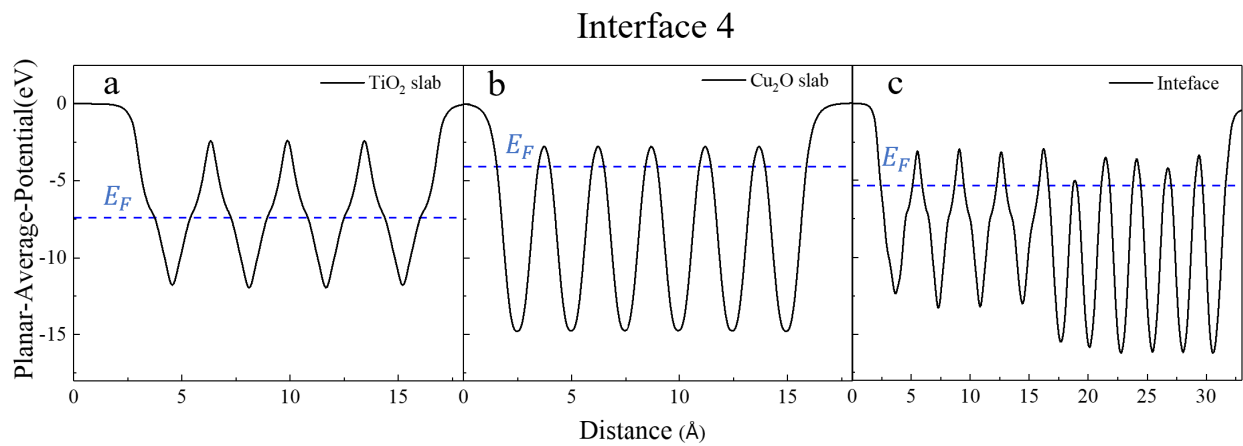


Figure 29. Fermi energy assessment of interface 4 (a,b) before and (c) after contact

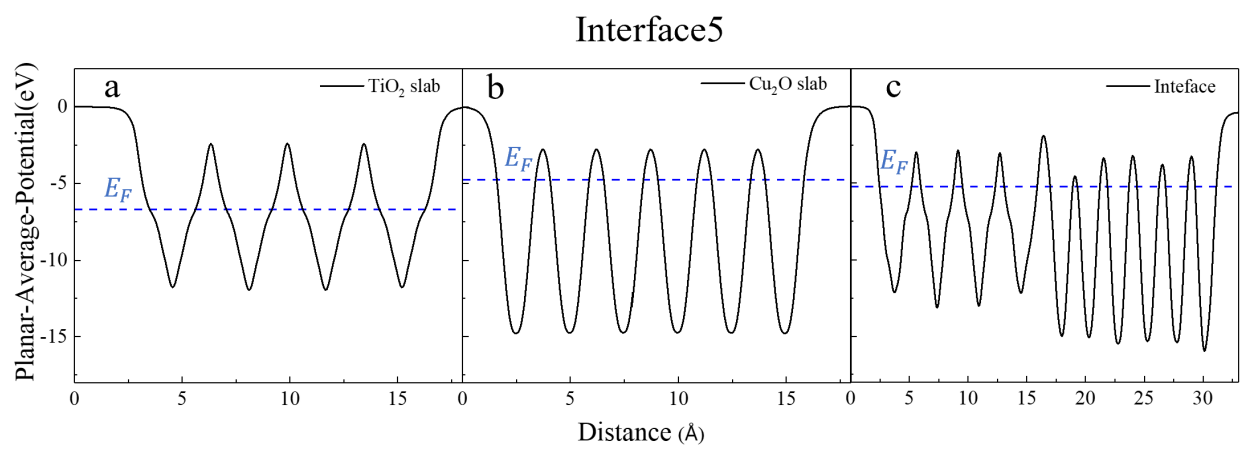


Figure 30. Fermi energy assessment of interface 5 (a,b) before and (c) after contact

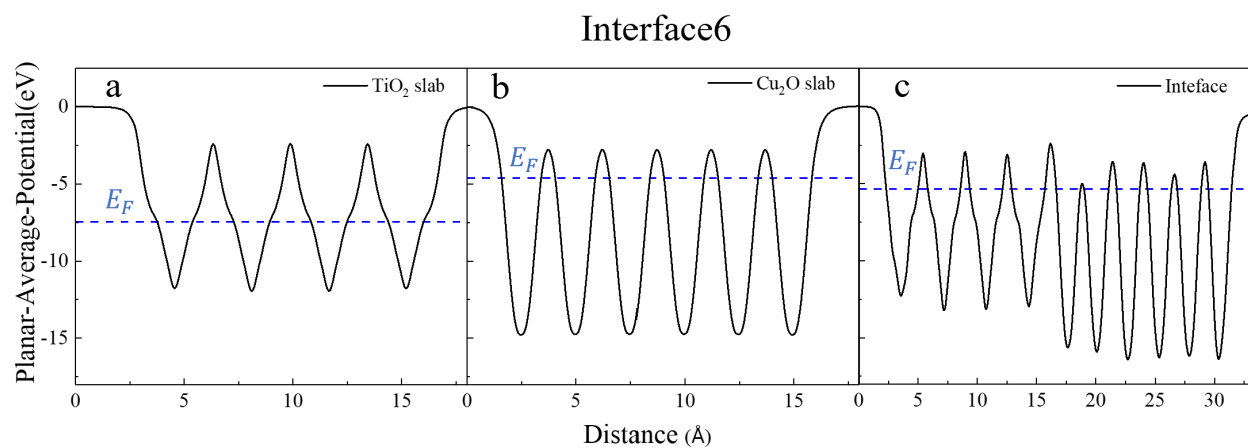


Figure 31. Fermi energy assessment of interface 6 (a,b) before and (c) after contact

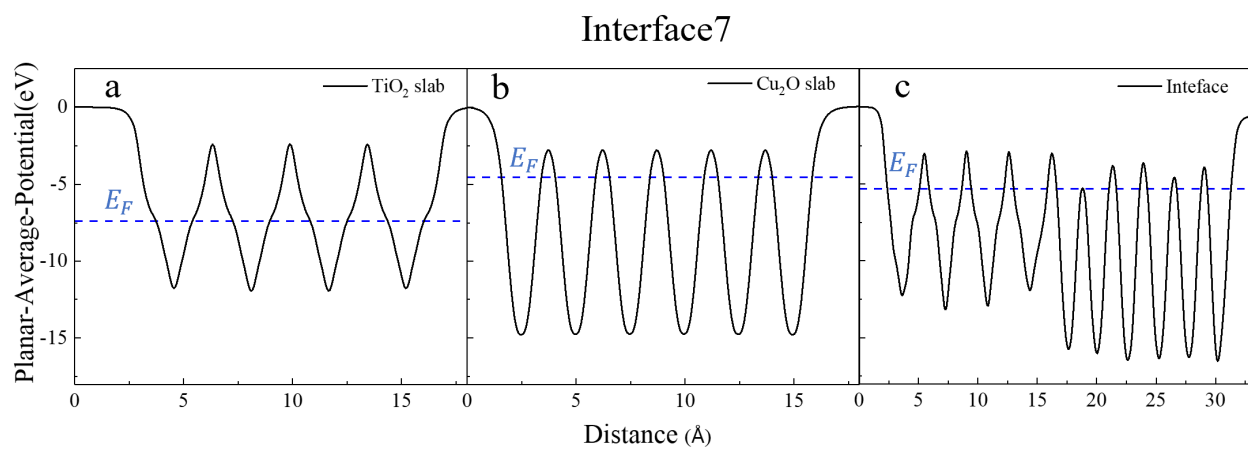


Figure 32. Fermi energy assessment of interface 7 (a,b) before and (c) after contact

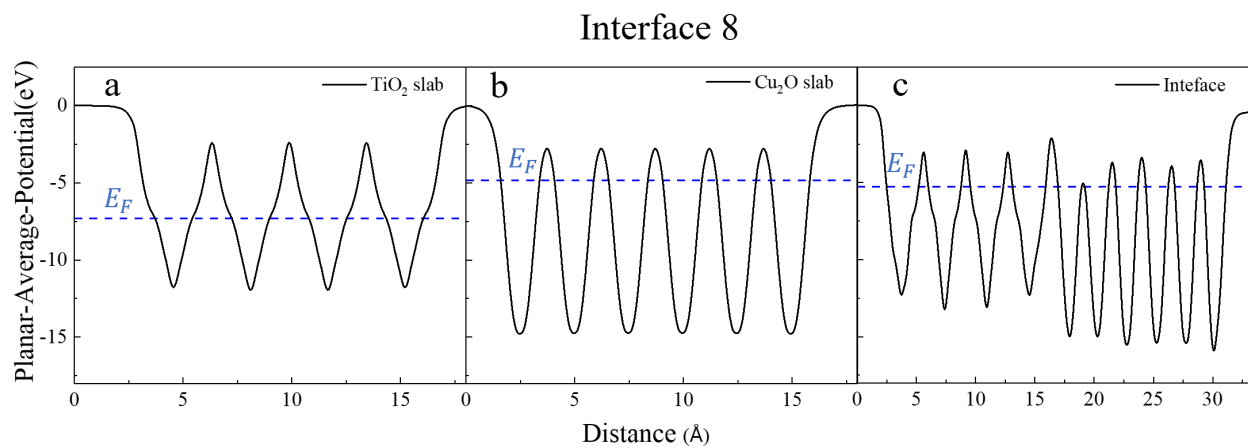


Figure 33. Fermi energy assessment of interface 8 (a,b) before and (c) after contact

References

- (1) Sawicka-Chudy, P.; Sibiński, M.; Rybak-Wilusz, E.; Cholewa, M.; Wisz, G.; Yavorskyi, R. Review of the development of copper oxides with titanium dioxide thin-film solar cells. *AIP Advances* **2020**, *10* (1). DOI: 10.1063/1.5125433 (accessed 1/29/2024).
- (2) Koffyberg, F. P.; Benko, F. A. A photoelectrochemical determination of the position of the conduction and valence band edges of p-type CuO. *Journal of Applied Physics* **1982**, *53* (2), 1173-1177. DOI: 10.1063/1.330567 (accessed 1/29/2024).
- (3) Kashiwaya, S.; Morasch, J.; Streibel, V.; Toupance, T.; Jaegermann, W.; Klein, A. The Work Function of TiO₂. *Surfaces* **2018**, *1* (1), 73-89.
- (4) Setvin, M.; Hulva, J.; Parkinson, G. S.; Schmid, M.; Diebold, U. Electron transfer between anatase TiO₂ and an O₂ molecule directly observed by atomic force microscopy. *Proceedings of the National Academy of Sciences* **2017**, *114* (13), E2556-E2562. DOI: doi:10.1073/pnas.1618723114.
- (5) Conesa, J. C. Modeling with Hybrid Density Functional Theory the Electronic Band Alignment at the Zinc Oxide–Anatase Interface. *The Journal of Physical Chemistry C* **2012**, *116* (35), 18884-18890. DOI: 10.1021/jp306160c.